Mémoire

Auteur : Fernandez Vera, Sorenza
Promoteur(s) : Rauw, Grégor
Faculté : Faculté des Sciences
Diplôme : Master en sciences spatiales, à finalité approfondie
Année académique : 2023-2024
URI/URL : http://hdl.handle.net/2268.2/21306

Université de Liège

Master Thesis

Phase-resolved X-ray spectroscopy of two colliding wind O-star systems

Master in Space Sciences

Author:
Sorenza FERNANDEZ VERA

Supervisor:
Gregor RAUW

Research Focus

16 August 2024

Acknowledgements

First of all, I would like to express my sincerest gratitude to my supervisor, Pr. Gregor Rauw. His invaluable guidance, the insights gained from our numerous discussions, and his constant availability have been essential in the completion of this thesis. His expertise have significantly enhanced my research experience, and I am grateful for his mentorship throughout this process.

Furthermore, I would like to extend my gratitude to my reading committee for the time they will dedicate to my work, namely Pr. Yaël Nazé, Pr. Damien Hutsemekers, and Dr. Ronny Blomme.

The quality of the lessons and the overall kindness of the teaching body of the Master in Space Sciences also deserve my gratitude. They aided me in developing self-assurance and an optimistic outlook regarding my future prospects.

In addition, I would like to convey my deepest thanks to my colleagues and friends from the Master's programme, the astrobees. The mutual support and the moments of laughter that punctuated our workdays were of great benefit to my mental health.

Furthermore, I want to express my deep gratitude to my close friends, Matilda D'Ermilio, Magali Limpens, and Iris Damoisaux, who have consistently been a source of support, particularly during periods of significant stress. I would also like to express my gratitude to my Erasmus partners, Clara Lonti and Julien Leclercq, who have provided invaluable encouragement and support throughout the year. They are undoubtedly the best people I have met this year. I want to acknowledge to my dear friend, Thomas Gerard, for his help with this project.

As this work marks the end of my studies, I would like to express my gratitude to my parents, who have consistently supported me. In particular, I am grateful to my mother for her patience and encouragement throughout my academic years, which have been a source of strength and inspiration.

Contents

Chapter 1

Introduction

> Gone is the classical conception of the Universe as a serene and majestic ensemble whose slow evolution is regulated by the consumption of the nuclear fuel. The Universe we know today is pervaded by the echoes of enormous explosions and rent by abrupt changes of luminosity on large energy scales. From the initial explosion to formation of galaxies and clusters, from the birth to the death of stars, high energy phenomena are the norm and not the exception in the evolution of the Universe.
>
> *Riccardo Giacconi*

This quote comes from one of the founding fathers of the X-ray astronomy, Riccardo Giacconi. More precisely, these are the last words of his Nobel lecture when he received the Prize in 2002 for "his pioneering contributions to astrophysics, which have led to the discovery of cosmic X-ray sources"[1]. Giacconi mentioned it after highlighting the crucial role of X-ray astronomy in the dynamics of the universe. Indeed, this field of study describes astrophysical processes in which matter has been heated to extremely high temperatures or in which particles have been accelerated to relativistic speeds.

This master thesis focuses on the analysis of Colliding Wind Binaries (CWBs), where the wind-wind interaction raises the temperature to several million Kelvin and therefore emission of X-rays. Specifically, the aim of this research is to describe the X-ray behaviour of two O-type binaries, HD168112, and HD167971[2] with a set of six XMM-Newton's observations over a period of two decades.

[1] He shared the Nobel Prize with Masatoshi Koshiba and Raymond Davis, Jr. for their work in neutrino astronomy.

[2] The prefix "HD" is a tribute to Henry Draper, an amateur astronomer who made a significant contribution to the field of astronomy. His widow made a donation to the Harvard Observatory, which enabled the study of a large sample of photographic stellar spectra, known as the "Henry Draper Catalogue".

This master thesis will be divided into four parts. In a first part, we will continue the introduction section with a presentation of the importance of studying O-type stars and their winds, with a focus on the colliding Wind Binary phenomena and an overview of the targets. Subsequently, a brief presentation of the XMM-Newton mission will be given, as well as of the instruments used. Follow by information about the observation and how they were processed. Thereafter, the results obtained will be presented. Finally, the results will be interpreted and discussed in the fourth part. In addition, the data will be compared with previous observations taken with the ROSAT satellite, and future perspectives will be given.

If they are not directly cited, the theoretical information presented in the following sections are derived from Rauw and Nazé [2015] and Rauw [2024], and references cited therein. Two distinct contributions to X-ray emission have been identified in binary systems. The first source is the thermal emission produced in the stellar winds of each individual star. The second source of X-ray emission is the colliding-wind region (CWR). In the next section we will begin by discussing the first contribution, which includes essential information about O-type stars. Subsequently, we will discuss the collision of the winds. Finally, a description of the targets will be provided.

1.1 O-type stars, their interest and their X-ray emission

O-types stars are massive stars ($M > 15\ M_{\odot}$), characterised by high temperatures ($T_{eff} > 30\ 000K$) which result in a scarcity of these stars, a relatively short lifespan following the stellar evolution process, and a high luminosity ($L_{Bol} > 10^4 L_{\odot}$). Despite their rarity, these objects are readily observable from considerable distances due to their luminosity. Moreover, their studies are of great importance, accorded to their significant role in the evolution of stars and their impact on the interstellar medium (ISM). As a result of their radiation field peaking in the ultraviolet, they effectively ionise the surrounding gases, leading to the formation of HII regions [De Becker and Van Grootel, 2023]. These gas clouds represent a phase of the ISM that drives the formation of others, which in turn give rise to the next generation of stars. In addition, they expel a considerable quantity of matter into the ISM throughout their lifetime, driven by their powerful stellar wind and at the final stages of their evolution (finishing as a supernova explosion). Consequently, the outflow of materials enriches the ISM and injects mechanical energy into it, impacting the dynamic and shape of it. These

initiates the self-contraction of these clouds, thereby triggering the star formation process. To give an idea of the matter and energy injected by the stellar wind of a main sequence O-type star, we can speak of a mass loss rate of approximately $2 \times 10^{-8} - 4 \times 10^{-6} M \odot yr^{-1}$ for an asymptotic wind velocity of around 2000-3000 km s^{-1}.

The X-ray spectra of massive stars display emission lines of highly ionised species. The intrinsic X-ray emission of non-magnetic O stars is described well by the line-deshadowing instability scenario (LDI). In order to understand this phenomenon, let's first consider a stable case. It is known that the charged particles (ions and electrons) which constitute the wind are subject to acceleration due to radiation pressure, with a resulting wind speed that takes the following form:

$$v = v_\infty (1 - \frac{R_*}{r})^\beta \tag{1.1}$$

Considering the phenomenon of photon absorption by an ion which occurs at a photon frequency $\nu = \nu_0(1 + v/c)$ due to the Doppler shift in the particle frame (where ν_0 is the transition frequency of the ion at rest). It is possible to discern a one-to-one relation between the spatial position of the ion (via relation (1.1)) and the frequency at which it absorbs photons. However, this mechanism is inherently unstable, as a slight perturbation in the ion's velocity can result in a complete alteration of its speed. These instabilities result in the formation of clumps of differing velocities, which subsequently undergo shocks within the wind. This results in shock-heated wind-embedded plasma, which then cools through the emission of X-ray photons via recombination.

The X-ray luminosity of O-type scales linearly with their bolometric luminosity following the relation $L_x/L_{bol} \sim 10^{-7}$ [Nazé, 2009]. This relation has been shown to be valid for O-star binaries, however strong wind interactions lead some systems to be overluminous in the X-ray domain.

1.2 Colliding Winds Binaries

The prevalence of multiple systems of O-type stars remains a subject of ongoing research. However, contemporary studies suggest that at least 71% of massive stars are in binary systems [Sana et al., 2012]. Their wind-wind interaction contributes significantly to their X-ray emission. Some massive binaries appear to exhibit an apparent overluminosity in comparison with others. This excess of luminosity in the X-ray domain is a direct consequence

of the colliding winds, which is why these objects are known as Colliding Winds Binaries (CWBs). The configuration proposed by Stevens et al. [1992] is as follows: The stellar wind from each star will form a hydrodynamic shock front with its surroundings. Consequently, two opposed shocks are formed, with an interaction zone between them constituted by the post-shock regions of each stellar wind, which is described as a shock cone. A contact discontinuity is present within the cone, separating the post-shock regions of the two stellar winds. The plasma is heated to temperatures approaching 10MK in the interaction zone and at the shocks particles can be accelerated through Diffusive Shock Acceleration (DSA) to relativistic velocities.

Regarding shocks, the prevailing theoretical framework is the Rankine-Hugoniot jump conditions. Presently, we are considering strong shocks (Mach number[3] $>$ 100) and the behaviour of monatomic gases. The Rankine-Hugoniot jump conditions of strong shocks are the following [De Becker and Van Grootel, 2023]:

$$\rho_{p-s} = \rho_{wind} 4 \tag{1.2}$$

$$P_{p-s} = \frac{3}{4}\rho_{wind} v_{\perp}^2 \tag{1.3}$$

$$kT_{p-s} = \frac{3}{16} m_{part} v_{\perp}^2 \tag{1.4}$$

In those relations ρ_{p-s}, P_{p-s}, and T_{p-s} are the density, the pressure and the temperature post-shock, ρ_{wind} and $v_{\perp}$ are respectively the density and the normal[4] speed of the wind (pre-shock), and m_{part} is the particle mass. The location and shape of the interaction zone are set by the wind momentum equilibrium condition expressed via the wind momentum ratio give by

$$\eta = (\frac{\dot{M}_1 v_{\infty,1}}{\dot{M}_2 v_{\infty,2}})^{1/2} = \frac{d_1}{d_2} \tag{1.5}$$

where $\dot{M}_i$, $v_{\infty,i}$, and d_i are respectively the mass-loss rate, the terminal velocity and the distance to the interaction zone of the component i. It should be noted that the assumption made is that the stellar winds will reach their constant terminal velocity before they collide, which is a valid assumption for wide binaries. In the case of two stars with an identical

[3]The Mach number is a quantity employed in the field of shock physics to express the strength of a shock. The Mach number is defined as $M = \frac{v_{wind}}{v_{sound}}$, where v_{wind} is the wind velocity before the shock and v_{sound} is the sound speed in the pre-shock zone.

[4]Normal to the front shock

momentum flux, the contact discontinuity is situated on a plane equidistant from both stars, as illustrated in Fig.1.1.

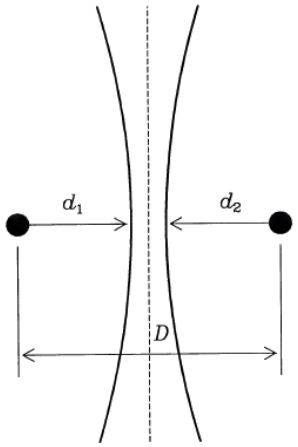

FIGURE 1.1: Schematic diagram of CWBs, assuming two identical stars separated by a distance D. d_1 and d_2 respectively represent the distance from each star to the nearest shocks front. The dashed line is the discontinuity line. Image taken from Stevens et al. [1992].

In contrast, for a system with a wind momentum ratio that differs significantly from one, the shock cone is observed to exhibit a curved morphology. In consequence, the contact discontinuity will be a curved surface, with the concave face oriented towards the star with the weaker wind. The Fig.1.2 displays hydrodynamic simulations with different values of η.

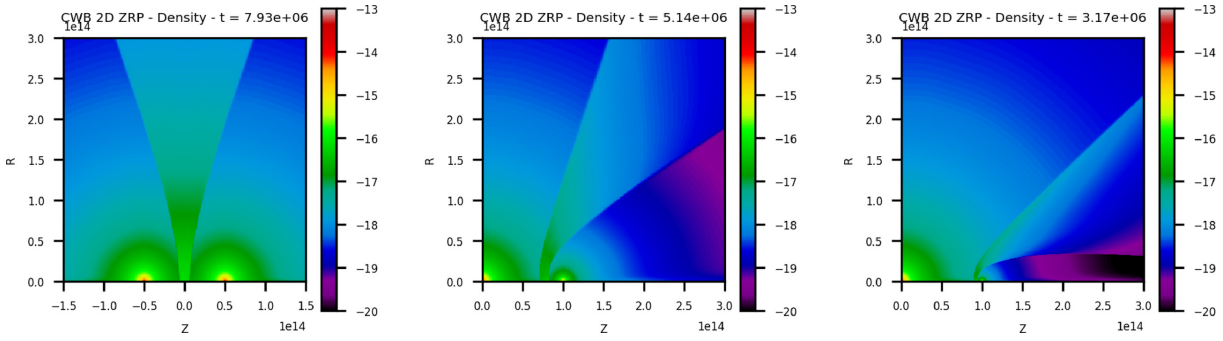

FIGURE 1.2: Hydrodynamic calculation performed by Pittard and Dawson [2018]. The display illustrates the interaction zone in an adiabatic system for various values of η. From left to right we have $\eta = 1.0$, $\eta = 0.1$, and $\eta = 0.01$.

We will now direct our attention to the interaction zone. We have a conversion of the kinetic energy into heat at the shock front. These results in a post-shock temperature[5] given by the eq.1.4. The shocked plasma inside the interaction zone will then cool down following either an adiabatic or a radiative regime. The former regime, in which the plasma cools adiabatically, occurs when radiative cooling is not efficient. This case is observed in the presence of low pre-shock density, resulting in a high post-shock temperature due to the prolonged recombination of ionised species. This phenomenon gives rise to a broad post-shock region, with long-period CWBs typically exhibiting this behaviour. In the radiative regime, the plasma cools rapidly, given its substantial energy loss. In this scenario, the density is sufficiently high to facilitate rapid recombination, resulting in a reduction in temperature compared to the adiabatic regime. Given the rapid cooling permitted by the high density, the shock region collapses and becomes much thinner compared to the adiabatic situation.

The aforementioned two cases are dependent on the properties of the inflowing material of the shock, and thus it is necessary to consider that this may differ for each component of the CWBs. The "cooling parameter" is the tool that allows us to ascertain which case we are in. It quantifies the efficiency of radiative cooling and is defined as the ratio of the timescale for radiative cooling to the escape time from the shock region. Stevens et al. [1992] approximated it with the expression:

$$\chi = \frac{t_{cool}}{t_{esc}} \approx \frac{v_8^4 d_{12}}{\dot{M}_{-7}} \tag{1.6}$$

where v_8 , d_{12}, and $\dot{M}_{-7}$ are respectively the wind velocity in 1000 km s^{-1}, the distance to the contact in $10^{12} cm$, and the mass-loss rate in $10^{-7} M_{\odot} yr^{-1}$. If we have $\chi >$1, the adiabatic regime holds, whilst we are in the radiative case if $\chi \ll 1$. The latter case usually occurs in close binaries because of higher density inside the winds. Note that, as said above, the regime can be different across the line of discontinuity, thus the χ have to be calculated for each shock.

The eq.1.4 shows that the orientation of the wind velocity will have an impact on the plasma temperature in the interaction area. Indeed, assuming that $v_{wind} = v_{\perp} + v_{\parallel}$, the maximum temperature will be reached when v_{wind} is nearly perpendicular to the shock ($v_{wind} \sim v_{\perp}$) which happens near the axis of the binary system. Subsequently, the temperature will

[5]The temperature immediately behind the shock

decrease along the cone as the $v_{\perp}$ decreases. This dissipation of the maximum temperature will have an impact on the temperature gradient. Furthermore, the temperature gradient is subject to additional complexity due to the discontinuity line, which gives rise to a distinct gradient across this line. Observed X-ray spectra are typically fitted with multiple discrete temperature models rather than a continuous range, in order to achieve a convergent fit. It is important to note that in reality this is not the case and that the plasma temperature varies from one position to another. The Fig.1.3 portrays this situation.

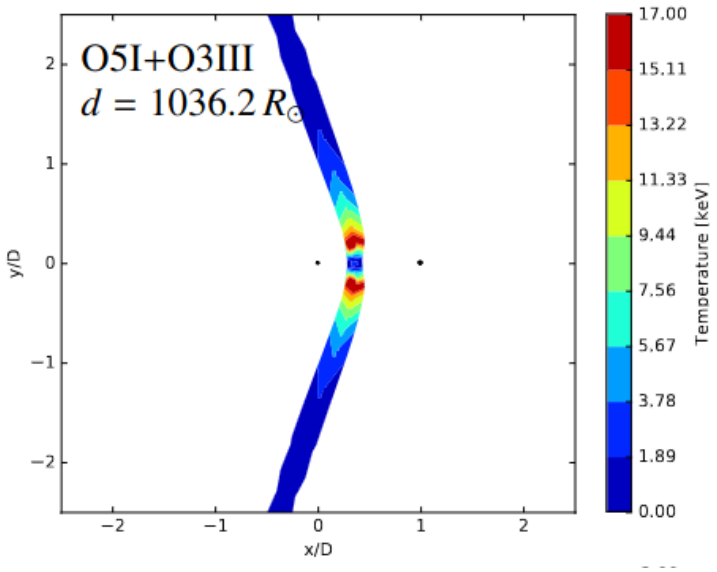

FIGURE 1.3: Hydrodynamic calculation performed by 2021AA...646A..89M. The simulation demonstrates the temperature gradient within the interaction zone. It can be observed that the maximum temperatures are expected close to the binary axis, though not directly on it, due to the influence of radiative braking.

Note that, following the eq.1.4, ions and electrons undergo different increases in temperature when they cross the shock front. In the case of a high-density interaction zone, the Coulomb and collision interactions between particles occur over a timescale shorter than the escape time, leading to an equalisation of the ion and electron temperature. However, this is not the case in low-density interactions, such as those observed in wide binaries, where these processes take much longer to occur. Therefore electrons (responsible for the bremsstrahlung continuum) and ions (producing emission lines) should have different radiation temperatures.

Moreover, the phenomenon of non-equilibrium plasma remains a complex subject that has yet to be fully explained.

The predicted X-ray emissions for O + O binaries were then confirmed by observation by the Einstein satellite. However, the observations revealed an emission intensity that was lower than anticipated. Since, significant progress has been made, mainly due to the insights gained from hydrodynamic simulations. The discrepancy between the theoretical predictions and the observational data has been partially explained by incorporating the effects of multiple processes that tend to reduce the strength of the shock. The effects of radiative inhibition and radiative braking, which result from the companion's radiation field, lead to a reduction in wind velocity and, thus, less energy is emitted. The 'communication' between the post and the pre-shock region due to relativistic particles will have a direct impact on the velocity jump. Indeed relativistic particles crossing the shock front forth and back exert a pressure from the post-shock region on the pre-shock gas (playing a role of precursor) and reducing the velocity shock jump. Furthermore, the temperature of the post-shock gas can be reduced through inverse Compton scattering of stellar photons. Moreover, CWB are subject to different instabilities. The three well-known are the thermal instability, the Kelvin-Helmholtz instability, and the Thin-Shell instability. They will deform the shape of the shock front and of the discontinuity line. These deformations will induce oblique shocks, which have a lower efficiency according to the same reasoning used above with the orientation of the velocity vector.

Over the past two decades, the capabilities of hydrodynamic simulations have reached their limits. To accurately simulate the full range of physical effects cited above, it is necessary to achieve high spatial resolution. This is particularly challenging in the context of instabilities, where reducing the cell size of the simulations, and consequently increasing the computational time, is essential. Problems were partially resolved using 3D adaptive-mesh based on a simulation with a variable cell size. This method permits us to have a better understanding of the impact of the gravity and orbital motion and thus the Coriolis deflection. Nevertheless, the issue of excessive computation times persists, necessitating the imposition of constraints such as the consideration of isothermal shocks.

As previously stated, the relation $L_x/L_{bol} \sim 10^{-7}$ remains valid for some CWBs, while others are overluminous in X-rays. The two cases of cooling provide insight into why some CWBs

are brighter than others in the X-ray range. In fact, when radiative cooling is highly efficient, thin-shell instabilities can occur as in the Fig.1.4. These instabilities shear the structure of shocks, leading to oblique shocks as said above. This explains why CWBs subject to this instability are not overluminous.

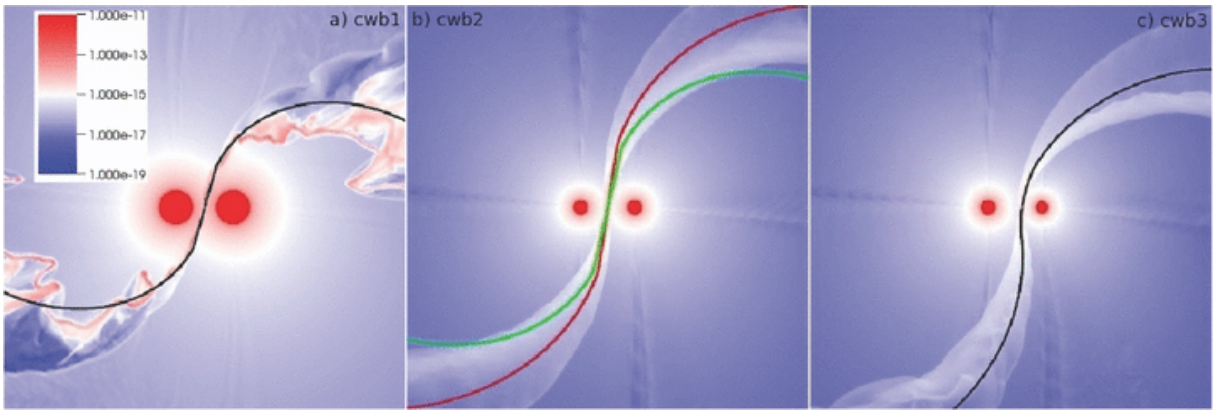

FIGURE 1.4: Hydrodynamic simulations performed by 2009MNRAS.396.1743P. From left to right, we got a radiative regime with two stars of the same spectral type (O6V + O6V), an adiabatic regime with two stars of the same spectral type (O6V + O6V), and an adiabatic regime with two stars of different spectral types (O6V + O8V). We can see the deformation of the shock cone in the radiative case.

CWBs display phase-locked variability of their X-ray emission of different origins. This can be caused by the change in the optical depth along the line of sight as the stars orbit each other. It is typically the case for eclipsing binaries. Then variability can come from the change of orbital separation in eccentric binaries. Combinations of both effects can also be seen. For eccentric binaries, we assume the flux to be dependent on the orbital separation. Under the adiabatic case, the X-ray emission, and therefore its flux, is expected to be proportional to $1/d$, with d the orbital separation between the stars.

1.3 Targets

This work will analyse observations of two O-type systems, HD168112 and HD167971. Both systems belong to the same open cluster NGC 6604, located in the Ser OB2 association.

Those systems are really interesting because of their multiple nature with rather long time-scales, which means that their studies are necessarily spread over several years. In addition, they are known to have a non-thermal signature in their spectra in the radio domain [Blomme et al., 2005, 2007]. Here is a presentation of each target.

1.3.1 HD 168112

This system has a right ascension of 18h 18m 40.867s and a declination of -12° 06' 23.367". Confirmation of the binarity of HD168112 has been given by Putkuri et al. [2023] who published a first orbital solution. Then recently by Blomme et al. [2024] who obtained similar results for the orbital parameters. The spectral type of Putkuri et al. [2023], and that will be used later in this work, is O4.5 IV ((f)) for the primary star and O.5.5 V(n)((f)) for the secondary. The ((f)) in the spectral type signifies that the spectrum presents the emission line of NIII at 4634-4640 Å and an absorption line of HeII at 4686 Å.

1.3.2 HD 167971

This system has a right ascension of 18h 18m 05.895s and a declination of -12° 14' 33.314". The system comprises three components: a short-period eclipsing binary, and a long-period third star. The orbital solution of the inner binary was given by Leitherer et al. [1987]. Evidence of the triple nature of HD167971 was provided for the first time by De Becker et al. [2012] with no orbital solution for the third component, which was provided by Ibanoglu et al. [2013]. Few years after, Le Bouquin et al. [2017] published a resolved astronomic orbit of the system. In this study, we will employ the spectral types presented by Ibanoglu et al. [2013] as a basis for our analysis. O7.5III for the primary, O9.5 III for the secondary, and O9.5 I for the third component of the system.

The Tables 1.1 & 1.2 show the orbital parameters that will be used later respectively for HD168112 and HD167971.

Parameter	Primary	Secondary
e	0.743 ± 0.005	
P [day]	513.52 ± 0.01	
T_{Peri} [HJD]	2455917.95 ± 0.49	
$a_i \sin_i$ [$R_\odot$]	478.1 ± 8.4	526.6± 4.3

TABLE 1.1: Orbital parameters of HD168112 following the work of Putkuri et al. [2023]. We used this article in our work instead of Blomme et al. [2024], as it was published at an earlier point in the academic year.

Parameter	Inner binary	Outer orbit
e	∼0	0.443 ± 0.020
P	3.321616 ± 0.000 002 [day]	7 806 ± 540 [day]
T	244 5554.9626 ± 0.0034 [HJD]	54 736± 59 [MJD]
a	36.69 ± 0.20 [$R_\odot$]	18.15 ± 0.90 [mas]

TABLE 1.2: Orbital parameters of HD167971 following the work of Ibanoglu et al. [2013] for the inner binary, and the work of Le Bouquin et al. [2017] for the outer orbit.

Chapter 2

Data Processing

All the information and figures given in the following section were extracted from the website of the European Space Agency [2024], the article of Jansen, F. et al. [2001] and the high energy course given by Rauw [2022].

2.1 The XMM-Newton Observatory

More than twenty years ago, the XMM-Newton observatory was launched by the Ariane V rocket, on the 10th of December in 1999. It is the second of the four cornerstones of the European Space Agency's (ESA) Horizon 2000 program, and remains one of the most important X-ray observatories. This mission was proposed to ESA in November 1982, then its objectives were settled during a workshop in June 1985, held in Lyngby in Denmark. The main goal was to perform high quality X-ray spectroscopy, especially on faint sources.

The satellite was put on an initial orbit with an eccentricity of 0.79 with the perigee altitude varying between 7000km and 22000km and the apogee altitude between 114000km and 100000km. The variations are explained by the evolution of the orbital parameters during the mission. For the high eccentricity, it was chosen for two main reasons. The first one was to operate outside the Van Allen radiation belts, in an environment with less high-energy particles. The second reason was to obtain a long operational time for observation. Indeed, XMM-Newton has an orbital period of 48h with 8 hours per orbit below the main radiation belt during which the instruments are switched off. We end up with 40 hours of operational time that allows long continuous observations.

The satellite is consisting of three X-ray telescopes and six instruments. In the following

subsection, we will present technical details concerning the mirrors, the instruments, and the spacecraft itself.

2.1.1 The telescopes

The satellite is composed of three Mirror Modules, which are grazing incidence telescopes. Each module comprises 58 gold-coated nested mirrors made of nickel. The design used for each of them is the so-called Wolter Type I, consisting of a paraboloid surface followed by a hyperboloid mirror. This configuration is effective for reducing the focal length, 7.5 m instead of 30 m if the mirrors were a single paraboloid type. The number of nested mirrors was chosen to achieve a relatively large effective area over an energy range of 0.1 to 10 keV. The maximum efficiency is approximately 1.5 keV with an absorption edge near of 2 keV (the Au M edge), see Fig.2.1.

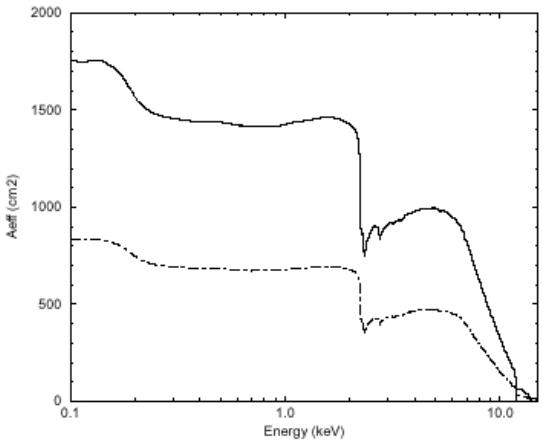

FIGURE 2.1: Graphic of the effective area as a function of the energy. The dot-dashed line is with RGA and the solid line without. Image taken from Jansen, F. et al. [2001].

In addition to the Mirror Modules, each telescope includes visible and X-ray baffles, and an electron deflector for diverting soft electrons. Furthermore, two of the three telescopes carry a Reflection Grating Array (RGA, see Sect.). The Fig.2.2 gives a schematic view of the telescope configuration.

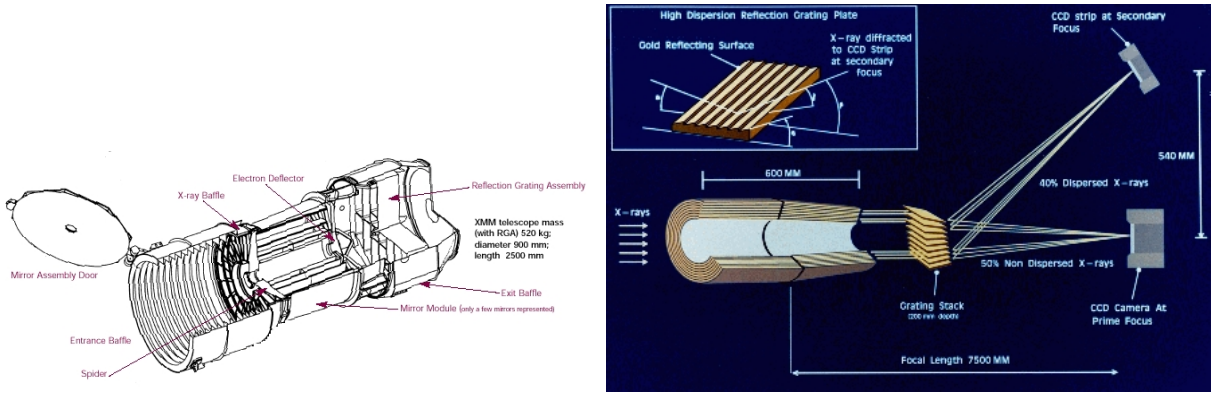

FIGURE 2.2: Left: Zoom on the mirror module configuration
Right: Schematic view of the light path in telescopes carrying an RGA.

The X-ray baffle is important for the background subtraction. Indeed, it reduces straylight photons from sources that are at an off-axis angle between 20' and 80'. Those photons are problematic as they reach the detector unfocused because of a single reflection from the rear end of the hyperbola. The X-ray baffles are placed in front of each mirrors module and are consisting of two sieves plates with 58 annular apertures.

2.1.2 The instruments

Six instruments were selected for the mission: three X-ray CCD cameras constituting the European Photon Imaging Camera (EPIC), two Reflection Grating Spectrometers (RGS), and the last one is the Optical Monitor (OM) operating in the UV and visible domain. The first five devices make it possible to obtain information on the incoming X-ray photons, their energy level and their time of arrival, in addition to their position for the EPIC detectors. The aim is to obtain spectra and images of the targets. As the instruments used for this work are the EPIC and the RGS, these will be well detailed. However, the OM, which was not used here, will only be described briefly.

2.1.2.1 The European Photon Imaging Camera

The EPIC cameras permit highly sensitive imaging observations in an energy range from 0.15 to 15 keV over a field of view (FOV) of about 30 arcmin diameter with a spectral and an angular resolution (PSF)[1] respectively of $E/\Delta E \sim 20 - 50$ and 6 arcsec.

[1]The Point Source Function describes the shape and size of the image of a point-like source.

The basic principle of Charge Coupled Device (CCD) detectors is based on the photoelectric effect. These instruments are made of semiconductors that generate photon-electrons when a photon strikes them. These electrons can be collected and their number will be proportional to the energy of the incident photon. There are two different CCD technologies on board the XMM-Newton: MOS (Metal Oxide Semiconductor) CCDs and PN CCDs. Both are three-phase frame transfer devices, nevertheless the main difference between them is that the EPIC-MOS devices are front-illuminated and the EPIC-PN camera is back-illuminated. The latter technology was new at the time of the launch. It was therefore decided to use it on only one of the telescopes, leaving the MOS on the other two for safety reasons. However, it is now well known that the back-illuminated CCDs are more sensitive to shorter wavelengths than the other, as the material is too thin to absorb longer wavelengths. The MOS CCD chips are located at the focal point of the X-ray telescopes that carry an RGA. Only 44% of the incoming light reaches the MOS detectors as a part of the photons is deviated to be directed on the RGS detector, as shown on the Fig.2.2. The EPIC-PN camera receives therefore more light, on average 2 times, being placed behind an unobstructed telescope. Here are some details about the geometry of the cameras.

For the EPIC-MOS CCDs, the instruments are constituted of seven EEV type 22 front illuminated CCDs. One is located at the center, at the focal point on the optical axis, and is surrounded by the other six (see Fig.2.3). These are stepped toward the telescope by 4.5mm in order to improve the PSF for off-axis sources.

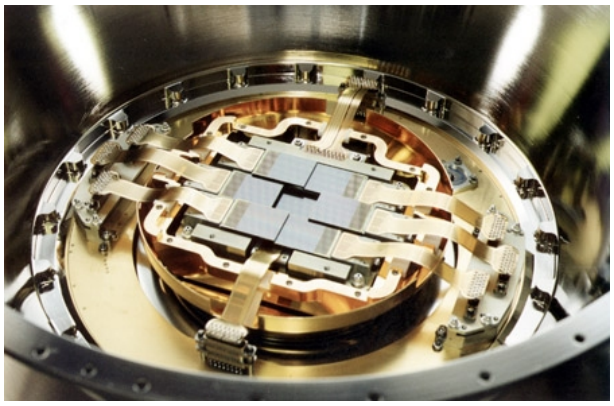

FIGURE 2.3: View on the EPIC-MOS camera array.

For the EPIC-PN detector, the camera is mounted on a single wafer in a monolithic

way. It consists of twelve pn CCDs arranged in two rows of six. Each CCD has a size of 3 x 1 cm, giving an imaging area of 6 x 6 cm. The instrument is divided into four quadrants sub-units, each consisting of three CCDs. The Fig.2.4 displays the geometry of the pn camera, it shows the internal boundaries as well. Approximately 97% of the FOV it is covered by the imaging area, about the 6 cm^2 remaining are used to study the background.

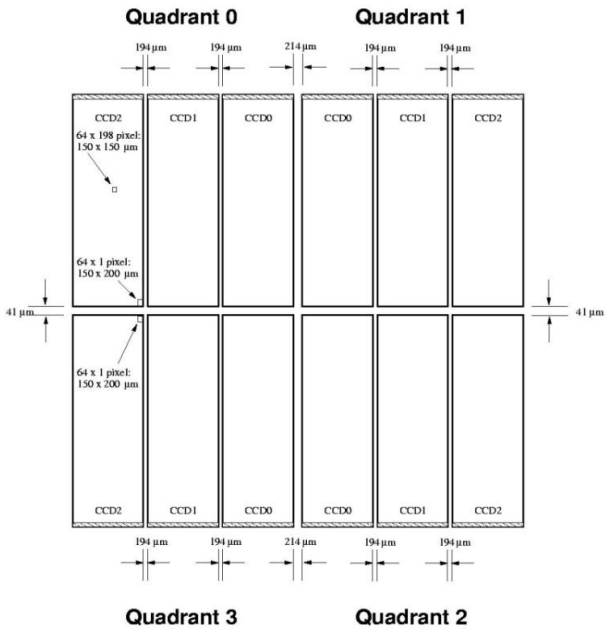

FIGURE 2.4: Schematic view of the EPIC-PN camera. The focal point is located on the quadrant 1 CCD 0.

A major problem with X-ray CCDs is that infrared, optical and UV light are all within their sensitive range and contaminate the X-ray signal. To reduce this issue, each EPIC camera is equipped with aluminised optical blocking filters. Six different filter setups are available on each filter wheel: two thin filters, a medium filter and a thick filter, an open position and a closed position. The thin filters are made of 1600 Å of poly-imide film with 400 Å of aluminium evaporated on it. For the medium filter, the constitution is the same as for the thin one with just the aluminium layer being thicker (800 Å). The last filter is formed of 3300 Å thick Polypropylene with 1100 Å of aluminium and 450 Å of tin evaporated on the film. The closed position is used to protect the detectors from soft protons. Finally, the open position is in principle for observation of sources with optical fluxes that are so low

that no filter is necessary. Using filters will affect the effective area, as the Fig.2.5 shows.

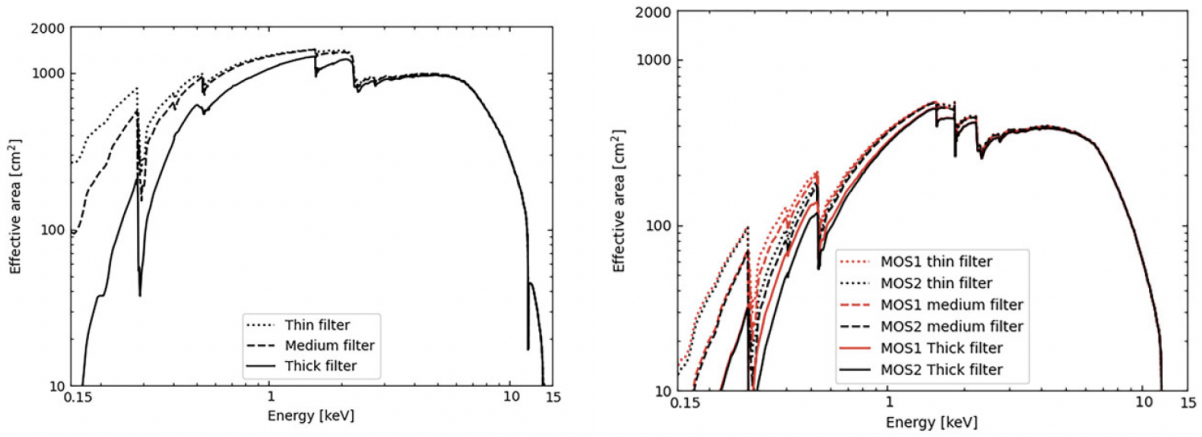

FIGURE 2.5: Graphic of the effective area as a function of the energy with filters, for the EPIC-PN camera on the left, and the EPIC-MOS on the right. We can see that the sensitivity of the MOS 2 is slightly under the one of the MOS 1. It is probably because of some contamination by hydrocarbons.

We also note that the EPIC instruments are also equipped with another experiment that is the EPIC Radiation Monitor (ERM). It is mainly used to monitor the particle environment to enable the proper functioning of the EPIC detectors.

To conclude with the EPIC instruments, they have suffered five accidents since the start of the mission, with varying degrees of damage. Three events left only minor after-effects, mainly faulty pixels. However, the two remaining events caused the loss of EPIC-MOS1 CCD 6 and EPIC-MOS1 CCD 3, in addition to a column of hot pixels located near of the EPIC-MOS1 boresight.

2.1.2.2 The Reflection Grating Spectrometer

This instrument disperses the light along the spatial direction, giving us information about the energy of each photon. As explained previously, the RGS shares a part of the optical path of the MOS detectors. It has an energy range from 0.33 to 2.5 keV with a peak of the effective area around 0.83 keV. About half of the out-coming light of the telescope will be diffracted by a grating stack mounted at grazing incidence. The photons are then focused to a strip of CCDs. The grating stack is the RGA, one is composed of 182 identical gratings and

the other one of 181 because of a problem during the installation. It consists of a support structure of a monolithic plate, hot-pressed under vacuum, with a SiC substrate of 1 mm, and a gold coating of 2000 A. For the groove density, it is approximately 646 grooves/mm, this number is at the centre and varies by 10% in order to avoid aberrations, which occur if the density is constant. Actually, the RGA are disposed on a Rowland circle that includes the mirror focus and the first order blaze focus, see the layout on the Fig.2.6.

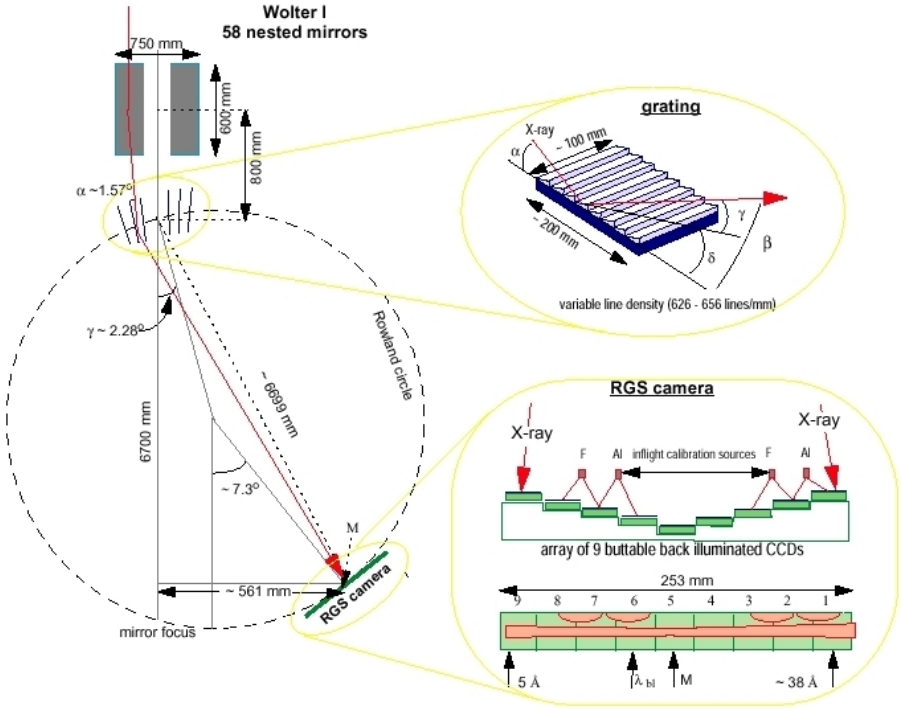

FIGURE 2.6: Schematic view of the RGS disposition.

The difference between the incident and reflected angles, α and β on the Fig.2.6, leads to a vignetting effects on the out-axes part of the FOV. For that reason, the RGS are used only when the target is located at the centre.

The focal plane camera (RFC) is composed of a row of nine back-illuminated CCDs working in single photon counting. This CCD bench follows the curvature of the Rowland circle. The RFC contains two heatshields, which permit to maintain it at a constant temperature of -80°C. The calibration is made thanks to internal sources contained in one of the shields (the alpha-emitter 244Cm, and an Al target or a Teflon target, they produce Al K alpha at 1487 eV and F K alpha at 676.8 eV fluorescent line emission). Once again, the use of

filters is essential to reject the optical light. It consists of a MgF_2 isolation layer above the substrate and an Al layer covering the CCDs with different thicknesses along the diffraction bench.

2.1.2.3 The Optical Monitor

The OM was integrated to the mission with the goal to perform observations in the ultraviolet/optical band simultaneously with the X-ray observations. The telescope is a Ritchey-Chretien type with an aperture of 30cm (primary mirror of 0.3 m and a hyperboloid secondary mirror). It covers a wavelength range from 170 to 650 nm and has a 17 arcmin square field of view.

The Tables 2.1, 2.2, 2.3 group main characteristics of the EPIC and RGS instruments and of the mirrors.

EPIC camera	PN	MOS
Type of CCD	back-front	Front
Number of CCDs	12	7
Imaging area	6 x 6 cm	2.5 x 2.5 cm
Fraction of light intercepted	100%	$\sim$ 44%

TABLE 2.1

RGS	
type of CCD	Back-front
angle of incidence α	12
angle of diffraction β_{blaze}	1.5762°
radius of the Rowland circle	2.9739°
Fraction of light intercepted	$\sim$ 51%
Energy range	0.33-2.5 keV
Substrat	SiC
Coating	Gold

TABLE 2.2

Mirrors parameters	
Focal length	7600 mm
Number of mirrors per telescope	58
Mirror substrate	Nickel
Reflective coating	Gold

TABLE 2.3

2.1.3 The spacecraft and its payload

With a width of 10m and a weight of around 4 tons, XMM-Newton is one of the largest scientific satellites ever launched by the ESA. The structure of it is mainly divided in four

components:

1. The Mirror Support Platform: carrying the three mirror assemblies (Mirror Modules + entrance and exit baffles + doors + two RGS grating boxes), the Optical Monitor (OM) and the two star-trackers.

2. The Focal Plane Assembly (FPA): the Focal Plane Platform (FPP) consisting of the focal-plane instruments: the RGS readout camera, the EPIC PN and MOS 1 & 2 imaging detectors. In addition there are radiators, allowing them to cool down the CCD detectors via cold fingers.

3. The Telescope Tube: the tube maintains the relative position between the FPA and the MSP. It's divided in two parts, the upper tube and the lower tube. The former includes two reversible venting and outgassing doors (VOD), and the outgassing baffle (OGB).

4. The Service Module: it is there that the spacecraft subsystems and associated units providing the necessary resources to the satellite are located.

The two solar-array wings, the Telescope Sun Shield (TSS) and the two S-band antennas are attached to the SVM part. Here is a visualisation of the spacecraft on Fig.2.7.

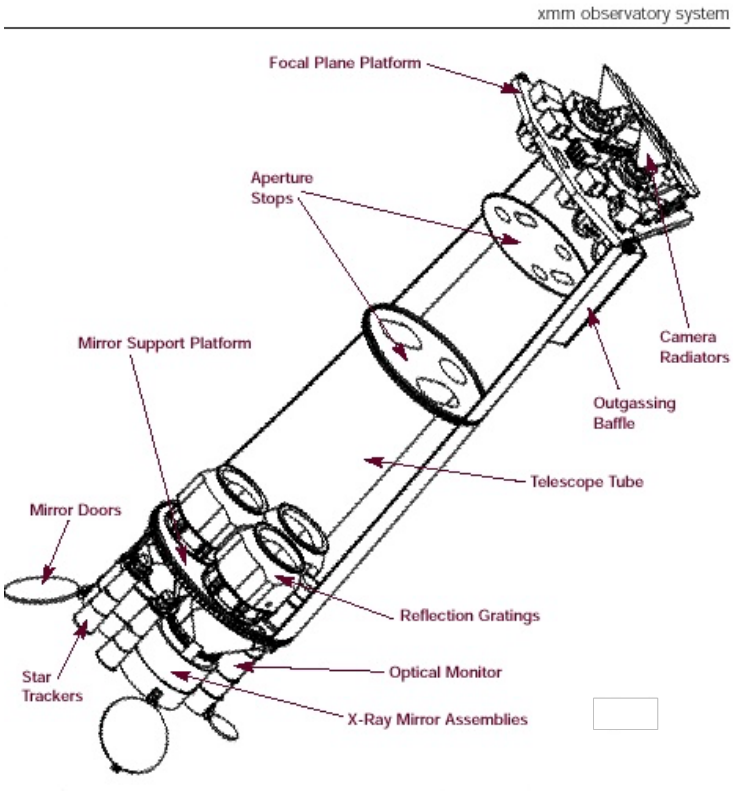

FIGURE 2.7: Schematic view of XMM-Newton payload.

2.2 Observations

The targets of our study belongs to the same open cluster and fall into a single EPIC field of view, allowing observing them simultaneously. The two systems have been observed at six different dates by XMM-Newton with different configurations of the field of view. The Table 2.4 shows information about these observations. During the first two, in 2002, the telescope pointed at a position between the stars. For Obs 3, in 2014, the observation was centred on HD167971. For the last three ones, HD 168118 was at the centre. The aim of those last observations was to observe the system near (Obs 4-6) and at the periastron (Obs 5) of HD168112. The instruments used were the PN , MOS 1 & 2, in full-frame mode in addition to the RGS when one source was in the centre. Due to the different configurations and some bad columns affecting detectors, all three EPIC instruments are not used for each observation. The Table 2.5 lists which instruments were used for a given observation.

Observ. ID	Observ. abbrev.	Date	Duration of the observ.	Main target
0008820301	Obs 1	07/04/2002	03h48min53s	HD 168112 & HD 197971
0008820601	Obs 2	09/09/2002	3h52min31s	HD 168112 & HD 197971
0740990101	Obs 3	09/09/2014	07h08min37s	HD 167971
0920040401	Obs 4	06/03/2023	3h35min16s	HD 168112
0920040501	Obs 5	22/03/2023	3h18min34s	HD 168112
0920040601	Obs 6	07/04/2023	3h18min38s	HD 168112

TABLE 2.4: parameters of XMM-Newton observations

	HD 168112			HD 167971		
	MOS 1&2	PN	RGS	MOS 1&2	PN	RGS
Obs 1	✓	✗	✗	✓	✗	✗
Obs 2	✓	✗	✗	✓	✓	✗
Obs 3	✓	✓	✗	✓	✓	✓
Obs 4	✓	✓	✓	✓	✓	✗
Obs 5	✓	✓	✓	✓	✓	✗
Obs 6	✓	✓	✓	✓	✗	✗

TABLE 2.5: instruments used for each observation.

We know the configuration of the systems by retrieving the orbital phase α. Using the Julian day (taken at the middle of each observation) to obtain the phases of each observation and the orbital solution of Putkuri et al. [2023] for HD168112, Ibanoglu et al. [2013] for the eclipsing binary of HD167971, and Le Bouquin et al. [2017] for the long period of HD167971. The orbital phases are then converted into true anomalies Φ via the eq.2.1 and the expression of the variable E (eq.2.3-2.4-2.5)[Rauw, 2023]. The Tables 2.6 & 2.7 give an overview of the system configuration of HD168112 and of HD167971. The distances, calculated with the eq.2.5, are the separation between the stars for HD168112, and between the inner binary

and the third component for HD167971.

$$E - e\sin E = \frac{2\pi(t-t_0)}{P_{orb}} = \alpha 2\pi \quad (2.1)$$

$$\cos\Phi = \frac{\cos E - e}{1 - e\cos E} \quad (2.2)$$

$$\sin\Phi = \frac{\sqrt{1-e^2}\sin E}{1 - e\cos E} \quad (2.3)$$

$$\tan\frac{\Phi}{2} = \sqrt{\frac{1+e}{1-e}}\tan\frac{E}{2} \quad (2.4)$$

$$r = \frac{a(1-e^2)}{1 + e\cos\Phi} \quad (2.5)$$

Obser.	Julian day	Phase HD168112	True anomaly [rad]	Distance [$R_\odot$]
Obs 1	2452372.56	0.096	2.226	938.43
Obs 2	2452526.79	0.396	2995	1938.83
Obs 3	2456909.73	0.931	2.016	755.51
Obs 4	2460009.81	0.968	1.443	469.46
Obs 5	2460025.98	0.999	0.064	295.03
Obs 6	2460042.45	0.032	1.443	469.46

TABLE 2.6: Orbital and observation parameters of HD168112.

Obser.	Julian day	$Phase_{ext}$ HD167971	True $anomaly_{ext}$ [rad]	$Distance_{ext}$ [$R_\odot$]	$Phase_{int}$ HD167971
Obs 1	2452372.56	0.697	1.87	6753.27	0.493
Obs 2	2452526.79	0.717	1.99	7177.84	0.925
Obs 3	2456909.73	0.278	3.85	8838.82	0.448
Obs 4	2460009.81	0.675	1.71	6266.73	0.751
Obs 5	2460025.98	0.678	1.73	6311.55	0.620
Obs 6	2460042.45	0.680	1.75	6367.43	0.580

TABLE 2.7: Orbital and observation parameters of HD167971.

2.3 High Energy Data

The data reduction was performed using the dedicated XMM-Newton software, the XMM-Newton Scientific Analysis System (SAS). It is developed by a team of scientists at ESA's XMM-Newton Sciences Operation Centre (SOC) and the XMM-Newton Survey Sciences Centre (SSC). The version of SAS used in this work is 1.3 XMMsas_20230412_1735-2102. The data reduction consists of six steps: calibration, data processing, grade filtering, flare detection, source detection, and spectrum extraction. Here is a summary of each step with the specific task and parameters used for the EPIC instrument process [2]:

1. **Calibration**: After retrieving the observation data file (ODF) from the XMM-Newton science archive, the calibration was performed using the cifbuild and odfingest tasks. The former retrieves the observation information, analyses it and selects the calibration files appropriate for the data and groups them in the calibration index file (CCF.cif). The odfingest task extracts information from the instrument housekeeping files and the calibration database and incorporates and then extends the ODF summary file into the SAS summary file. These files contain all the necessary information for SAS to process the data sets.

2. **Data processing**: To process the EPIC data sets we used the two tasks of the SAS package epicproc: epproc and emproc for the EPIC instruments. The former is a pipeline for the EPIC PN data files, the latter for the EPIC MOS 1 and 2 data files. The Fig.2.8 shows how the PN pipeline works, and ends with the output datasets: the imaging event, the attitude housekeeping, and the list of bad pixels.

3. **Grade filtering.**: We applied event thresholds and pattern selections. The default events selections used are the following: for the PN instrument "FLAG = 0 and PATTERN <= 4", for the MOS instruments "#XMMEA_EM and PATTERN <= 12". The #XMMEA and FLAG = 0 conditions remove all events close to the CCD gap or bad pixels. The PATTERN conditions are restrictive regarding the shape of the detection cell around the pixel with the highest number of free electrons. The different pattern codes are shown in the Fig.2.9 for MOS1-2 on the left and on the right for the PN. The limitation of the shape allows keeping only compact and isolated elements which have the highest probability to correspond to a genuine X-ray photon.

[2](information taken from the "Users Guide to the XMM-Newton Science Analysis System", Issue 18.0, 2023 (ESA: XMMNewton SOC).

4. **Flare detection**: Light curves of each observation were made to identify possible background flares. These were produced by selecting all events above 10 keV and using a 0 pattern and a time binning of 100s. For the PN instrument, an additional condition was implemented to take events below 12 keV to avoid thermal noise being misidentified as an event. Two flares were detected in the data analysed in the work. The first at the end of Obs 1. The second at the beginning of Obs 3. Then, using the command Tabgtigen, the Good Times Intervals (GTI) files are created, excluding the observation period with a count rate above a given value (O.2 for the EPIC MOS 1 & 2, and 0.4 for the EPIC PN). The GTI were usd (for Obs 1 and 3) to produce cleaned event lists which select the events filtered with the criteria defined in step 3 according to an additional criterion which is their time of arrival. The light curves of the Obs 1 is given in the Fig.2.10.

5. **Source detection**: The source selection was made based on images that account for the good time intervals and contain photons in the range of 0.3 keV to 10 keV. The task used to perform the source detection is edetect_chain. It created an exposure map which provides the effective exposure time for each position within the field of view. The detected sources are then overplotted on a mosaic built by combining sky images from all three EPIC cameras.

6. **Spectrum extraction**: The extraction of the spectrum is divided into 3 steps: definition of the source and background, production of the spectra and generation of the .pi files. The definition of the extraction region is done based on the Gaia coordinates of stars and adopting a circle of 600 pxl radius and the background in an annulus centred on the source with an inner radius of 600 pxl and an outer radius of 1000 pc. When extracting the spectrum of HD167971 from Obs 5, the pn instrument showed a few columns of bad pixels close to the centre of the source. In order to perform the extraction correctly, a box mask was created with a width of 120 pxl and a length of 1000 pxl. The task especget produces all the spectral products: source and background spectrum, the RMF (redistribution matrix file) and the ARF (ancillary response file). Finally, the specgroup task performs a user-defined grouping of the channels in the spectrum and links the associated files to the .pi files used in the XSPEC software.

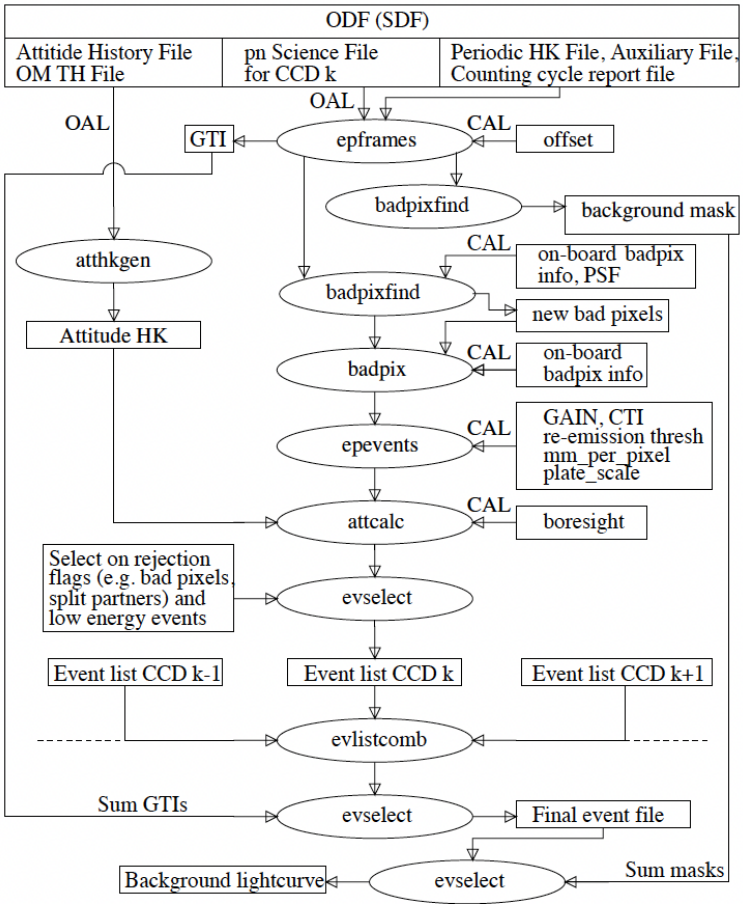

FIGURE 2.8: Pipeline processing diagram for the PN instrument. Image taken from the SAS on-line documentation.

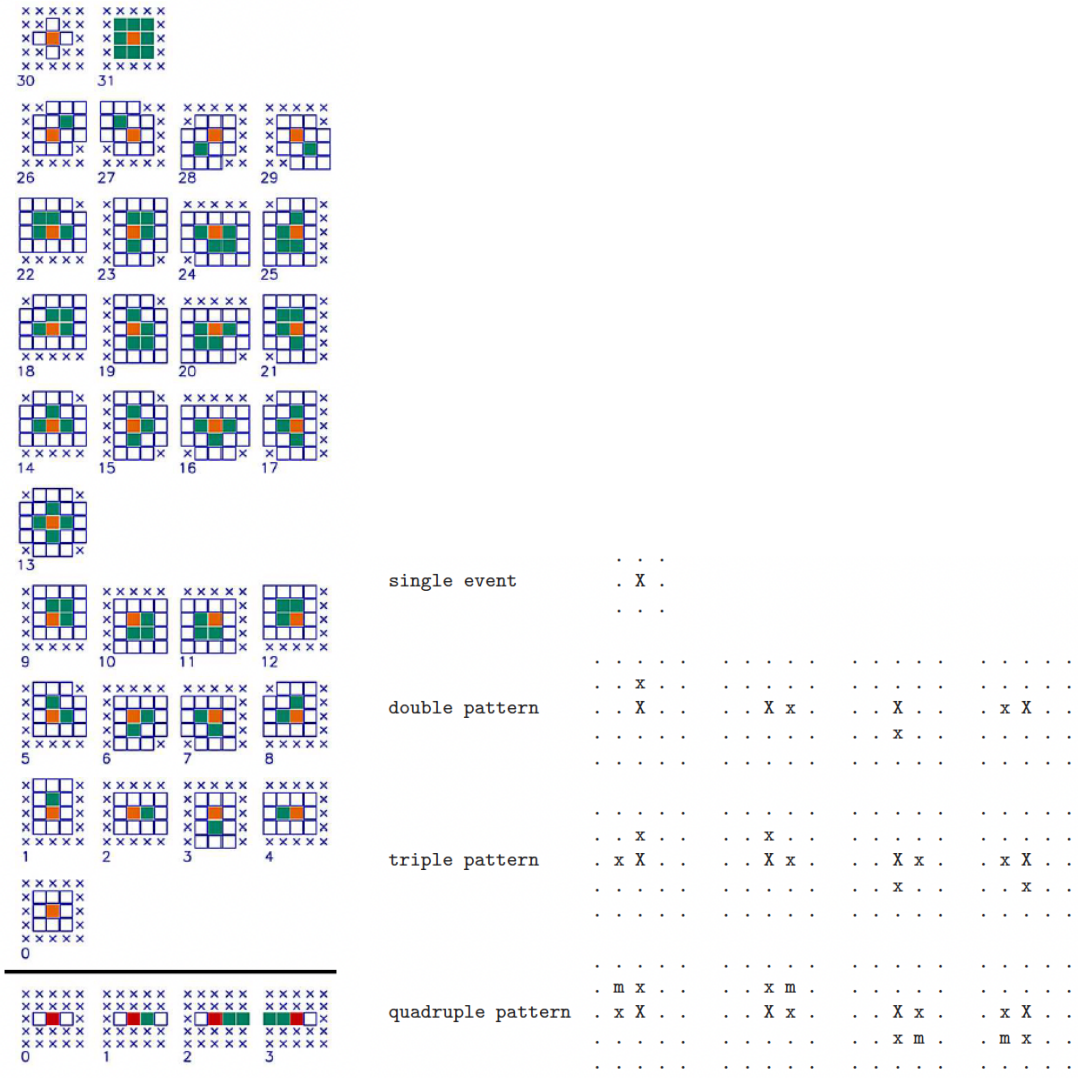

FIGURE 2.9: Left: pattern code of the MOS instruments. The orange boxes represent the main pixel that received the highest pulse impulse (PI), the green boxes are pixels with a PI higher than the detection threshold. Right: The dots are pixels with no detection, the X represents the main pixel, the x are the equivalent of the green boxes, and the m are events with the minimal PI detection. The pattern codes are respectively 0 (singles), 1-4 (doubles), 5-8 (triples) and 9-12 (quadruples). Images taken from the Users Guide to the XMM-Newton Science Analysis System.

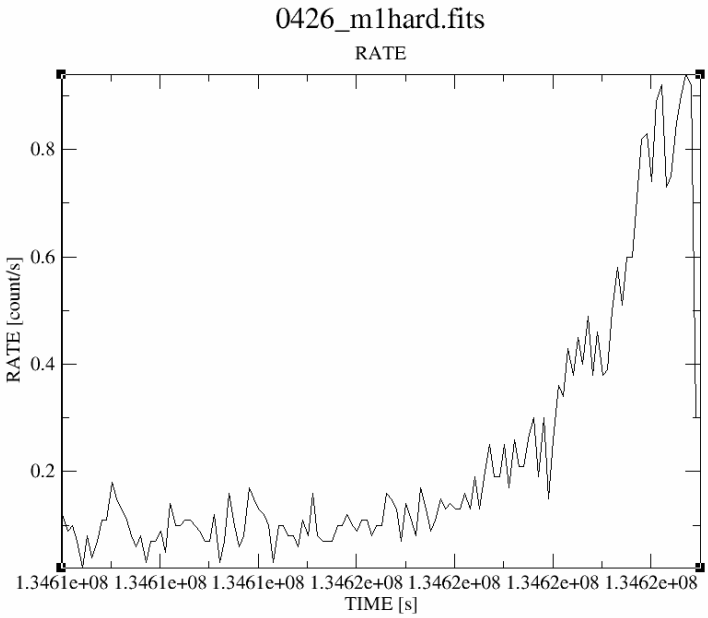

FIGURE 2.10: Background light-curve of the first observation.

RGS data reduction is similar to EPIC. The two RGS instruments capture light dispersed by a reflection grating along a spatial direction and recorded by an array of nine CCD cameras. The first and second orders of diffracted light are processed.
The calibration step is exactly the same as for the EPIC data. For the data processing, the task needed is rgsproc which works similarly to epproc and emproc (output datasets: the imaging event, the attitude housekeeping, and the list of bad pixels). The flare detection is directly integrated in the RGS reduction pipeline. The rule of thumb is to check the counts rate on the CCD number nine (values above 1 count/s will be excluded). Two flares were detected for the third and fourth observations. As for the EPIC flares, the command Tabgtigen permitted to selected the GTI, then the task rgsfilter merged them in our data. Then we visualised our data thanks to the task rgsimplot. Two plots are generated, one of the photon energies and one of the spatial dimensions, both as a function of first order wavelength converted from the spatial position. As the Fig.2.11 shows, the RGS instruments received a low level of light. We extracted the spectrum using task rgsspectrum on each order of each RGS. Then we used task rgsrmfgen to create the RMF. Finally, we used specgroup to obtain the .pi files. We end up with four RGS spectral files for each observation (RGS1 order1, RGS1 order 2, RGS2 order 1,RGS2 order 2).

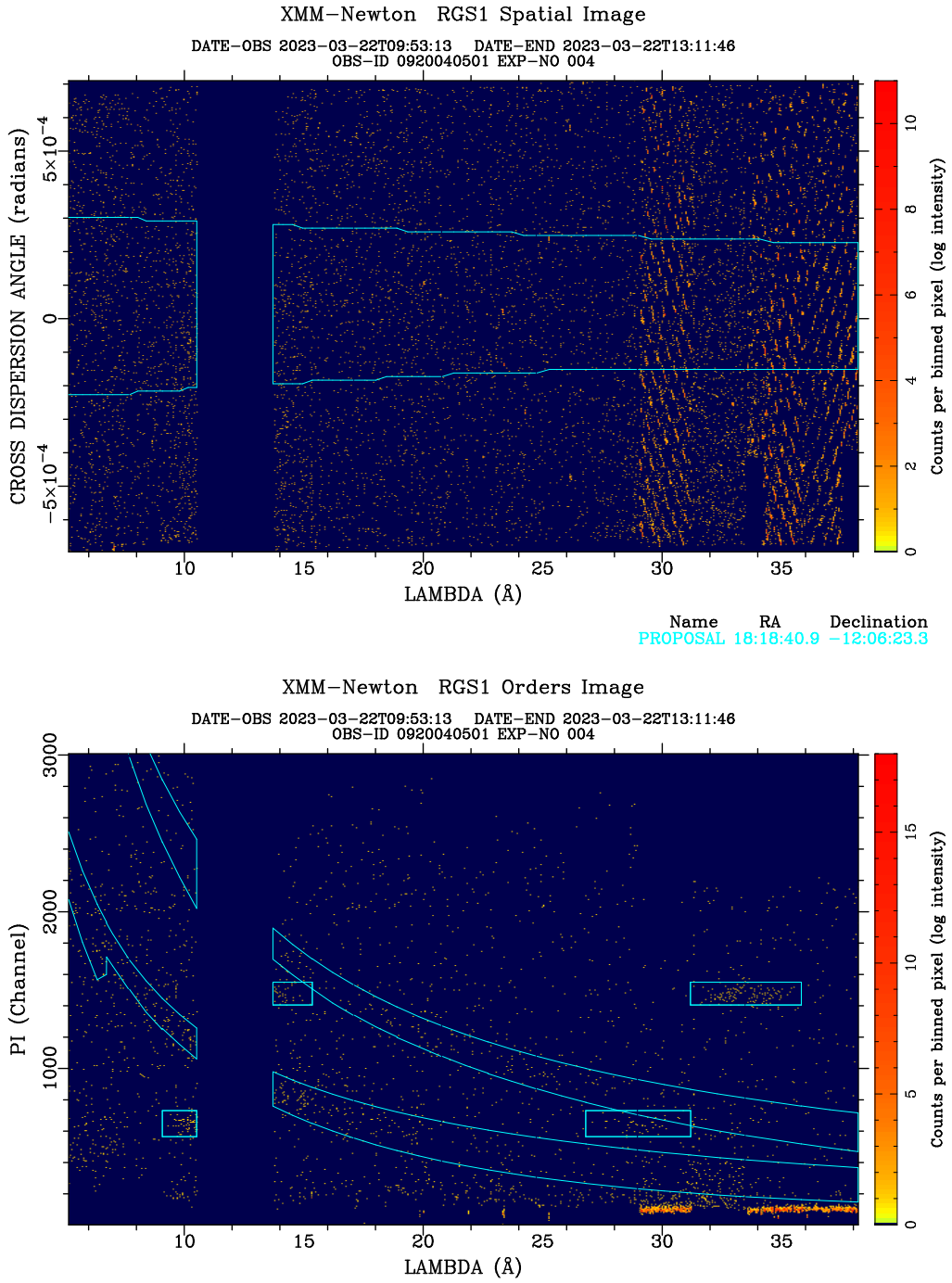

FIGURE 2.11: The top shows the spatial dimension perpendicular to the dispersion direction as a function of wavelength. The bottom shows the photon energy as a function of wavelength, also called a "banana plot". The figure corresponds to the RGS1 data of the fifth observation. The curved cyan areas in the bottom panel indicate the location of the first order (lower curved area) and the second order (upper curved area).

Chapter 3

Results

In this section, the results of the six observations will be presented. We start by outlining the methodology adopted to construct models that fit with the observed data, allowing us to infer the spectral properties and fluxes of the systems. We subsequently present the methodology employed to derive the cooling parameters for each colliding wind component and the calculations of the X-ray luminosity. Finally, we describe the procedure by which a three-colour image of the field of view around the targets was created.

3.1 Spectral fitting

With the .PI files obtained in the previous section, we attempt to fit the spectra with models using absorption components related to the interstellar medium and the stellar winds, combined with optically thin thermal plasma models. For this purpose we use the Xspec software. We firstly use a model of the type TBabs*phabs*(apec+apec) on the EPIC-MOS1, EPIC-MOS2, EPIC-PN data, with the addition of the RGS1 and RGS2 data when they are available. We set the plasma chemical abundances to solar following the value of Asplund et al. [2009] with the abund command. Here is an explanation of the different components of the model. The TBabs component takes into account the photoelectric absorption of X-rays by the interstellar medium. The name stands for the Tuebingen-Boulder ISM absorption model, and it is the sum of the cross sections for X-ray absorption due to the gas-phase, the grain-phase, and the molecular hydrogen in the ISM. For HD168112, the ISM column density parameter was frozen and set to a value of $0.575 \times 10^{22} cm^{-2}$ taking an average value of $N_H = 0.58 \times 10^{22} \times E(B-V) cm^{-2}$ [Bohlin et al., 1978], and $N_H = 0.58 \times 10^{22} \times E(B-V) cm^{-2}$ [Gudennavar et al., 2012], an intrinsic colour $(B-V)_0 = -0.28$ using an O5III(f) spectral type [Martins et al., 2005], and an observed colour index $B-V = 0.69$ [Ducati, 2002]. The relation of Bohlin et al. [1978] and Gudennavar et al. [2012] express the mean ratio between

neutral hydrogen gas and reddening due to dust in the Galactic interstellar medium.

The phabs component stands for the circumstellar photoelectric absorption of X-rays. It represents the absorption due to the wind material and is a free parameter. The (apec + apec) component represents the thermal X-ray emission spectrum from an optically thin plasma heated by hydrodynamic shocks (either intrinsic to the stellar winds or due to the colliding winds). The number of apec models in the sum is the number of different plasma temperatures we assume, and they are also free parameters. Our first model uses two plasma temperatures, it will be referred to as the 2T model.

We use the same model for HD167971. This time, we set the ISM column density to 0.515×10^{22} computed for an intrinsic colour $(B-V)_0 = -0.22$, assuming an O8Ib(f) spectral type [Martins et al., 2005], and an observed colour index $B-V = 0.60$ [Ducati, 2002]. The best fit model parameters for our observations can be found in the Table 3.1 for HD168112, and in the Table 3.3 for HD167971. Those parameters are the circumstellar absorption columns (N_h^{circum}), the temperature multiplied by the Boltzmann constant (kT_i), and the normalisation parameter which is given by $\frac{10^{-14}}{4\pi D_A^2} \int n_e n_H \, dV$ where D_A is the angular diameter distance to the source (cm), dV is the volume element (cm^3), and n_e and n_H are the electron and H densities (cm^{-3}), respectively.

The ratio of the Chi squared to the number of degrees of freedom of the observation 5 clearly shows that the 2T model is not the optimal one. We thus tested a three temperatures model (3T model). An F-test confirms that it is better suited to fit our data. We end up with a set of parameters for the 3T model summarised in Table 3.2 for HD168112, and in the Table 3.4 for HD167971.

Observation	N_h^{circum} $10^{22}cm^{-2}$	kT_1 (keV)	N_1	kT_2 (keV)	N_2	Chi^2/dof
Obs1	$0.715\ ^{+0.195}_{-0.218}$	$0.258\ ^{+0.061}_{-0.045}$	$5.99\times10^{-3}\ ^{+9.5}_{-3.7}\ \times10^{-3}$	$2.623\ ^{+1.138}_{-0.635}$	$3.97\times10^{-4}\ ^{+8.8}_{-8.5}\ \times10^{-5}$	59.7/67
Obs2	$0.274\ ^{+0.156}_{-0.255}$	$0.596\ ^{+0.093}_{-0.122}$	$4.8\times10^{-4}\ ^{+2.5}_{-3.0}\ \times10^{-4}$	$4.898\ ^{-4.897}_{-2.214}$	$1.66\times10^{-4}\ ^{+7.3}_{-5.6}\ \times10^{-5}$	58.72/65
Obs3	$0.711\ ^{+0.137}_{-0.141}$	$0.266\ ^{+0.043}_{-0.040}$	$5.51\times10^{-3}\ ^{+2.56}_{-7.03}\ \times10^{-3}$	$2.085\ ^{+0.336}_{-0.285}$	$7.51\times10^{-4}\ ^{+8.7}_{-7.6}\ \times10^{-5}$	157.89/157
Obs4 EPIC	$0.786\ ^{+0.123}_{-0.118}$	$0.257\ ^{+0.033}_{-0.034}$	$9.56\times10^{-3}\ ^{+4.13}_{-9.73}\ \times10^{-3}$	$2.218\ ^{+0.222}_{-0.194}$	$8.85\times10^{-4}\ ^{+7.9}_{-7.3}\ \times10^{-5}$	243.43/217
Obs4 EPIC+RGS	$0.751\ ^{+0.117}_{-0.111}$	$0.268\ ^{+0.031}_{-0.032}$	$7.79\times10^{-3}\ ^{+6.66}_{-3.11}\ \times10^{-3}$	$2.224\ ^{+0.218}_{-0.188}$	$8.78\times10^{-4}\ ^{+7.3}_{-6.9}\ \times10^{-5}$	455.06/451
Obs5 EPIC	$0.563\ ^{+0.106}_{-0.113}$	$0.285\ ^{+0.035}_{-0.029}$	$5.93\times10^{-3}\ ^{+2.31}_{-3.65}\ \times10^{-3}$	$1.875\ ^{+0.195}_{-0.152}$	$1.104\times10^{-3}\ ^{+0.83}_{-0.86}\ \times10^{-4}$	333.18/231
Obs5 EPIC+RGS	$0.574\ ^{+0.105}_{-0.108}$	$0.281\ ^{+0.030}_{-0.031}$	$6.11\times10^{-3}\ ^{+3.73}_{-2.26}\ \times10^{-3}$	$1.856\ ^{+0.161}_{-0.176}$	$1.11\times10^{-3}\ ^{+0.09}_{-0.07}\ \times10^{-3}$	626.28/491
Obs6 EPIC	$0.427\ ^{+0.089}_{-0.104}$	$0.656\ ^{+0.041}_{-0.061}$	$1.09\times10^{-3}\ ^{+0.29}_{-0.26}\ \times10^{-3}$	$3.284\ ^{+1.305}_{-0.724}$	$3.97\times10^{-4}\ ^{+0.99}_{-0.89}\ \times10^{-5}$	230.19/193
Obs6 EPIC+RGS	$0.457\ ^{+0.075}_{-0.093}$	$0.627\ ^{+0.048}_{-0.050}$	$1.19\times10^{-4}\ ^{+2.70}_{-3.22}\ \times10^{-4}$	$3.239\ ^{+1.201}_{-0.689}$	$4.05\times10^{-4}\ ^{+0.96}_{-0.88}\ \times10^{-4}$	455.33/419

TABLE 3.1: Best-fit parameters for the spectra of HD168112 using the 2T model. N_h^{circum} is the circumstellar absorption column, given in $10^{22}cm^{-2}$.

Obs.	N_h^{circum}	kT_1 (keV)	N_1	kT_2 (keV)	N_2	kT_3 (keV)	N_3	Chi^2/dof
Obs1	$0.687^{+0.197}_{-0.220}$	$0.206^{+5.296}_{-0.075}$	7.47×10^{-3} $^{+36.54}_{-5.79}$ $\times10^{-3}$	$0.530^{+8.37}_{-0.463}$	0.63×10^{-3} $^{+1.14}_{-0.63}$ $\times10^{-3}$	$3.348^{+5.564}_{-3.349}$	0.31×10^{-3} $^{+0.13}_{-0.12}$ $\times10^{-3}$	57.30/65
Obs2	$0.452^{+0.271}_{-0.132}$	$0.126^{+0.090}_{-0.088}$	13.52×10^{-3} $^{+212.40}_{-12.53}$ $\times10^{-3}$	$0.578^{+0.103}_{-0.134}$	0.59×10^{-3} $^{+0.27}_{-0.23}$ $\times10^{-3}$	$5.579^{-5.599}_{-2.811}$	0.16×10^{-3} $^{+0.08}_{-0.05}$ $\times10^{-3}$	51.41/63
Obs3	$0.675^{+0.146}_{-0.168}$	$0.238^{+0.041}_{-0.031}$	5.96×10^{-3} $^{+7.47}_{-3.34}$ $\times10^{-3}$	$1.277^{+0.198}_{-0.155}$	0.57×10^{-3} $^{+0.14}_{-0.19}$ $\times10^{-3}$	$8.162^{-9.050}_{-5.635}$	0.22×10^{-3} $^{+0.08}_{-0.18}$ $\times10^{-3}$	136.70/155
Obs4 EPIC+ RGS	$0.255^{+0.273}_{-0.210}$	$0.355^{+0.135}_{-0.077}$	0.66×10^{-3} $^{+2.19}_{-0.48}$ $\times10^{-3}$	$0.922^{+0.091}_{-0.064}$	0.35×10^{-3} $^{+0.13}_{-0.10}$ $\times10^{-3}$	$2.854^{+0.463}_{-0.311}$	0.61×10^{-4} $^{+0.07}_{-0.08}$ $\times10^{-5}$	425.88/449
Obs5 EPIC+ RGS	$0.426^{+0.166}_{-0.172}$	$0.275^{+0.053}_{-0.042}$	3.14×10^{-3} $^{+1.80}_{-4.70}$ $\times10^{-3}$	$1.002^{+0.137}_{-0.092}$	0.62×10^{-3} $^{+0.23}_{-0.14}$ $\times10^{-3}$	$2.818^{+1.292}_{-0.457}$	0.63×10^{-3} $^{+0.14}_{-0.22}$ $\times10^{-3}$	564.71/489
Obs6 EPIC+ RGS	$0.628^{+0.134}_{-0.145}$	$0.279^{+0.069}_{-0.046}$	3.34×10^{-4} $^{+4.17}_{-1.84}$ $\times10^{-4}$	$0.791^{+0.121}_{-0.103}$	0.64×10^{-3} $^{+0.34}_{-0.23}$ $\times10^{-3}$	$3.050^{+1.195}_{-0.622}$	0.43×10^{-3} $^{+0.11}_{-0.11}$ $\times10^{-3}$	425.30/417

TABLE 3.2: Best-fit parameters for the spectra of HD168112 using the 3T model. N_h^{circum} is the circumstellar absorption column, given in $10^{22}cm^{-2}$.

Observation	N_h^{circum}	kT_1 (keV)	N_1	kT_2 (keV)	N_2	Chi^2/dof
Obs1	$0.858\ ^{+0.120}_{-0.110}$	$0.310\ ^{+0.049}_{-0.042}$	$17.37\times10^{-3}\ ^{+6.65}_{-12.83}\ \times10^{-3}$	$1.896\ ^{+0.404}_{-0.301}$	$1.31\times10^{-3}\ ^{+0.25}_{-0.27}\ \times10^{-3}$	112.17/111
Obs2	$0.802\ ^{+0.077}_{-0.075}$	$0.263\ ^{+0.029}_{-0.027}$	$17.16\times10^{-3}\ ^{+5.18}_{-8.66}\ \times10^{-3}$	$1.331\ ^{+0.142}_{-0.098}$	$1.60\times10^{-3}\ ^{+0.17}_{-0.17}\ \times10^{-5}$	58.72/65
Obs3 EPIC	$0.410\ ^{+0.037}_{-0.039}$	$0.665\ ^{+0.015}_{-0.015}$	$2.20\times10^{-3}\ ^{+0.24}_{-0.27}\ \times10^{-3}$	$1.654\ ^{+0.079}_{-0.095}$	$1.10\times10^{-3}\ ^{+0.10}_{-0.08}\ \times10^{-3}$	622.21/346
Obs3 EPIC+RGS	$0.406\ ^{+0.035}_{-0.037}$	$0.665\ ^{+0.014}_{-0.014}$	$2.11\times10^{-3}\ ^{+0.27}_{-0.21}\ \times10^{-3}$	$1.596\ ^{+0.100}_{-0.052}$	$1.15\times10^{-3}\ ^{+0.10}_{-0.07}\ \times10^{-3}$	1307.07/972
Obs4	$0.366\ ^{+0.095}_{-0.087}$	$0.658\ ^{+0.042}_{-0.074}$	$2.467\times10^{-3}\ ^{+0.55}_{-0.80}\ \times10^{-3}$	$1.566\ ^{+0.193}_{-0.178}$	$1.37\times10^{-3}\ ^{+0.22}_{-0.22}\ \times10^{-3}$	215.55/181
Obs5 EPIC	$0.185\ ^{+0.058}_{-0.058}$	$0.715\ ^{+0.026}_{-0.026}$	$1.87\times10^{-3}\ ^{+0.32}_{-0.32}\ \times10^{-3}$	$1.569\ ^{+0.066}_{-0.066}$	$2.05\times10^{-3}\ ^{+0.12}_{-0.12}\ \times10^{-4}$	1163.64/186
Obs6	$0.771\ ^{+0.138}_{-0.149}$	$0.229\ ^{+0.045}_{-0.031}$	$30.84\times10^{-3}\ ^{+17.06}_{-38.18}\ \times10^{-3}$	$1.268\ ^{+0.146}_{-0.098}$	$2.91\times10^{-3}\ ^{+0.32}_{-0.37}\ \times10^{-3}$	103.96/108

TABLE 3.3: Best-fit parameters for the spectra of HD167971 using the 2T model, the circumstellar absorption column N_h^{circum} are given in $10^{22}cm^{-2}$.

Obs.	N_h^{circum}	kT_1 (keV)	N_1	kT_2 (keV)	N_2	kT_3 (keV)	N_3	Chi^2/dof
Obs1	$0.820^{+0.140}_{-0.149}$	$0.300^{+0.079}_{-0.054}$	$13.06^{+16.41}_{-7.33}\times10^{-3}$	$0.838^{+0.132}_{-0.122}$	$1.61^{+0.65}_{-0.69}\times10^{-3}$	$3.165^{+5.676}_{-1.036}$	$0.58^{+0.33}_{-0.28}\times10^{-3}$	95.79/109
Obs2	$0.846^{+0.107}_{-0.077}$	$0.145^{+0.027}_{-0.027}$	$88.04^{+242.48}_{-52.54}\times10^{-3}$	$0.390^{+0.081}_{-0.063}$	$6.38^{+4.01}_{-2.02}\times10^{-3}$	$1.596^{+0.331}_{-0.159}$	$1.22^{+0.20}_{-0.30}\times10^{-3}$	290.32/226
Obs3 EPIC+ RGS	$0.683^{+0.060}_{-0.048}$	$0.293^{+0.020}_{-0.020}$	$7.55^{+3.02}_{-1.88}\times10^{-3}$	$0.827^{+0.031}_{-0.032}$	$1.66^{+0.22}_{-0.18}\times10^{-3}$	$1.905^{+0.214}_{-0.146}$	$0.88^{+0.12}_{-0.13}\times10^{-3}$	1089.68/970
Obs4	$0.626^{+0.114}_{-0.132}$	$0.302^{+0.071}_{-0.040}$	$8.50^{+7.64}_{-4.58}\times10^{-3}$	$0.854^{+0.092}_{-0.079}$	$1.67^{+0.51}_{-0.46}\times10^{-3}$	$1.834^{+0.520}_{-0.272}$	$1.10^{+0.32}_{-0.33}\times10^{-3}$	172.73/179
Obs5	$0.449^{+0.087}_{-0.087}$	$0.265^{+0.029}_{-0.029}$	$6.78^{+3.57}_{-3.57}\times10^{-3}$	$0.819^{+0.057}_{-0.057}$	$1.87^{+0.34}_{-0.34}\times10^{-3}$	$1.519^{+0.113}_{-0.113}$	$1.99^{+0.26}_{-0.26}\times10^{-3}$	1145.67/184
Obs6	$0.584^{+0.205}_{-0.218}$	$0.268^{+0.088}_{-0.049}$	$9.80^{+22.12}_{-7.26}\times10^{-3}$	$0.923^{+0.220}_{-0.137}$	$1.63^{+0.84}_{-0.75}\times10^{-3}$	$1.660^{+6.498}_{-0.292}$	$1.48^{+0.99}_{-1.29}\times10^{-3}$	97.18/106

TABLE 3.4: Best-fit parameters for the spectra of HD167971 using the 3T model. N_h^{circum} is the circumstellar absorption column, given in $10^{22}cm^{-2}$.

The Fig.3.1 displays our best fits of the EPIC-MOS1, EPIC-MOS2 and EPIC-PN spectra of HD168112 in the case of the 3T model for the six observations. In the same configuration, the Fig.3.2 displays EPIC-MOS1,EPIC-MOS2 and EPIC-PN spectra of HD167971 in the case of the 3T model for the six observations. The plots for the 2T case can be found in the Appendix Sect.5. We note here that the first two observations of HD168112 lack the EPIC-PN data as the source was affected by gaps and bad columns of the PN detector. The same remark applies to the first and last observation of HD167971.

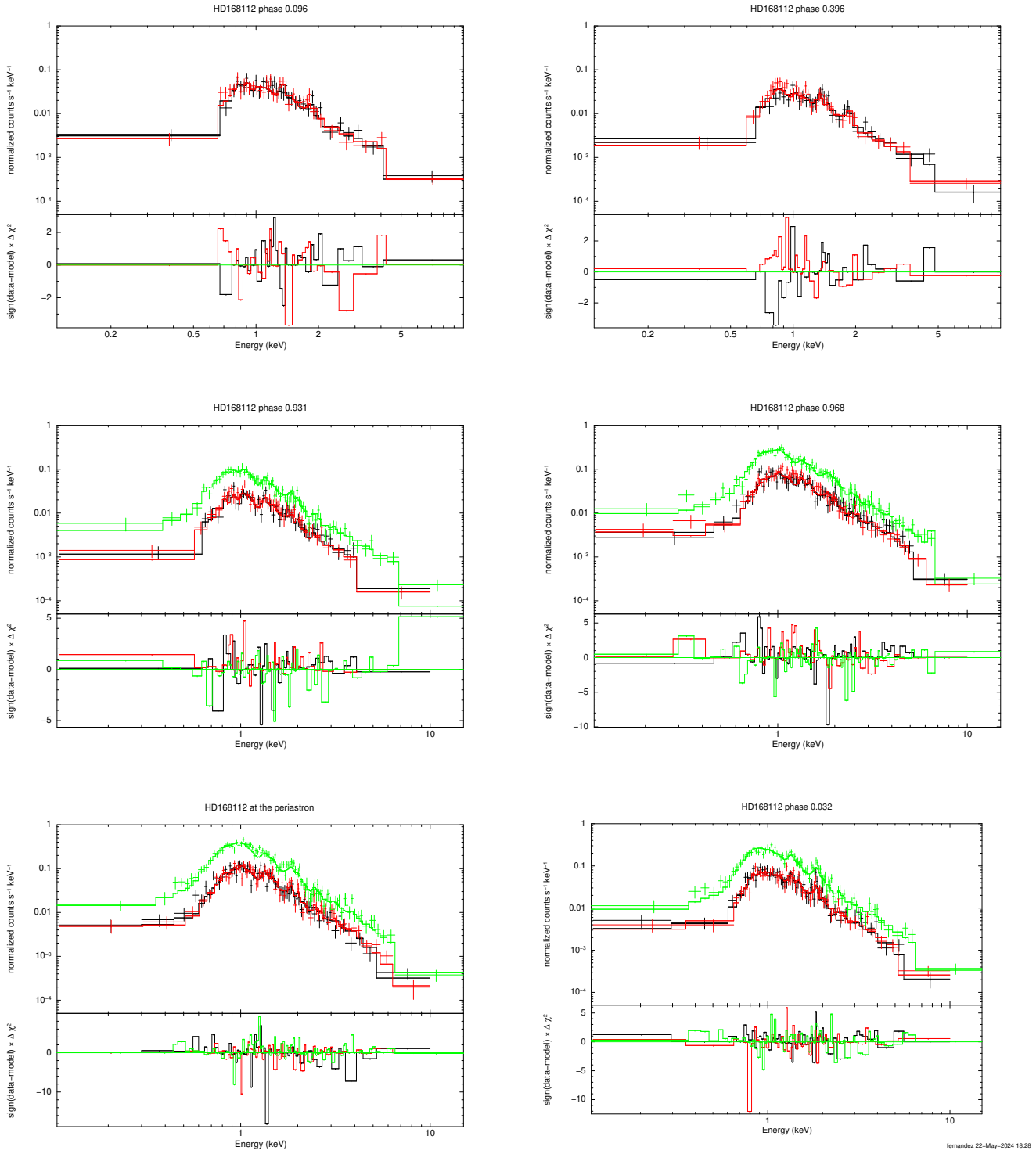

FIGURE 3.1: EPIC-MOS1 (in black), EPIC-MOS2 (in red) and EPIC-PN (in green) spectra of HD168112 in the case of the 3T model for the 6 observations. In the lower part of each graph, the deviation of the data set in comparison to the model is shown. From top left to bottom right, the different panels correspond to observations 1, 2, 3, 4, 5 and 6.

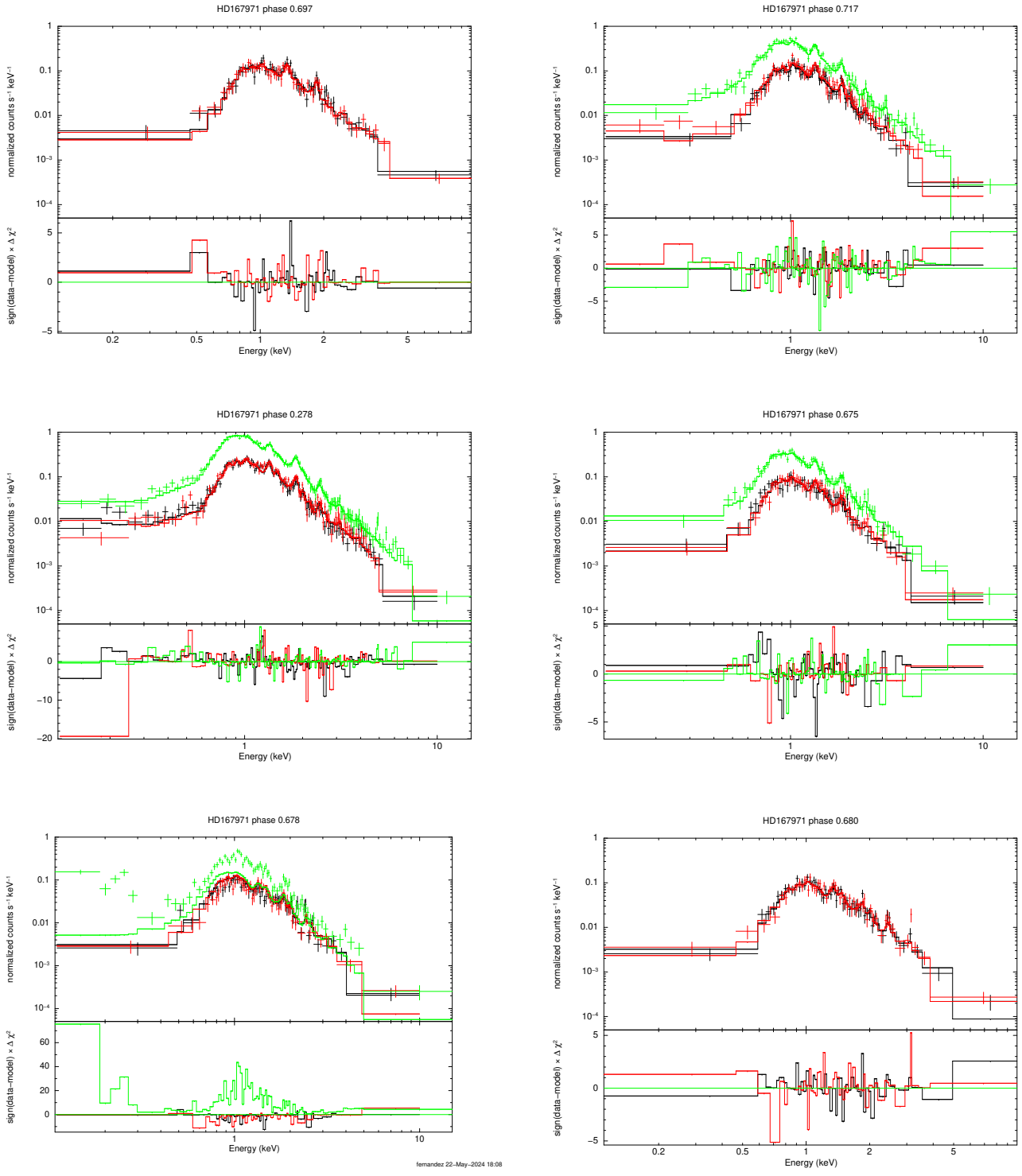

FIGURE 3.2: Same as Fig.3.1, but for the 3T models fitted to the spectra of HD167971.

3.1.1 Spectra analysis

We focus on a spectrum for each target. Some emission lines are clearly seen in the EPIC spectra. For HD168112, six have been identified for the Obs 4 (see Fig.3.3): Mg XI (1.34 keV), Mg XII (1.47 keV), Si XIII (1.85 keV), Si XIV (2.01 keV), S XV (2.45 keV) and S XVI (2.62 keV) cannot be deblended at the spectral resolution of the EPIC instruments, and Fe XXV (6.67 keV). The spectrum displays a broad emission complex due to multiple iron lines (we will call it the iron complex), O VII (0.57 keV), O VII (0.65 keV), Ne IX (0.91 keV), and Ne X (1.02 keV). The Fe XXV line, which indicates the presence of a very hot plasma, is visible only on Obs. 4, whilst we could have expected to observe it also on Obs. 5 which was taken at periastron, when the X-ray emission is the strongest. We come back to this point in Chap.4.

For HD167971, two additional emission features can be distinguished as shown by Fig.3.4: one consisting of the blend of the Ar XVII lines at 3.12 and 3.32 keV, and Ca XIX (3.88 keV). The broad emission zone is also present.

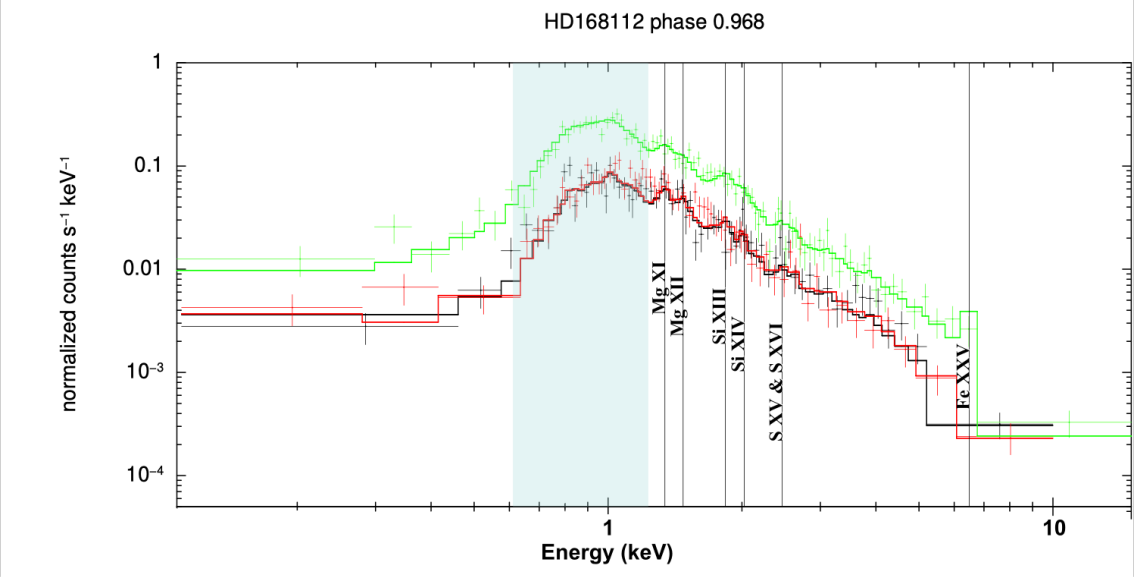

FIGURE 3.3: Spectrum of HD168112 of the fourth observation with the identified emission lines. The blue region corresponds to the blend of iron, oxygen and neon lines discussed in the text.

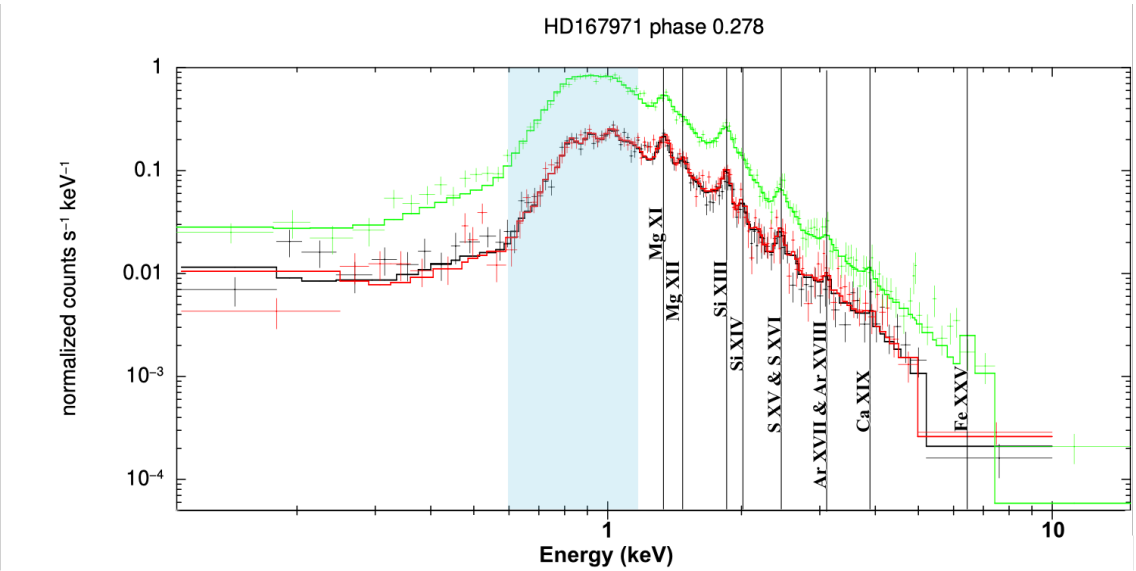

FIGURE 3.4: Spectrum of HD167971 of the third observation with the identified emission lines. The blue region corresponds to the blend of iron, oxygen and neon lines discussed in the text.

3.2 Spectral fluxes and their variations

Using the spectra of the 3T models, fluxes were retrieved and are given in the Table 3.5. These fluxes have been calculated in three different energy ranges: one in the soft part of the spectrum (from 0.5 to 1 keV), then in the harder part (from 1 to 10 keV), and finally taking into account the full energy range (from 0.5 to 10 keV). Then, we obtain the fluxes corrected from the ISM absorption from 0.5 to 10 keV. In order to do that, we set the column density of the TBabs to 0 but kept the column of the circumstellar Phabs absorption model to the one of the Table 3.2 for HD168112, and of Table 3.4 for HD167971. The errors on the fluxes were evaluated as 1σ (68% confidence range) error bars by means of the flux err command.

Obs.	Flux soft	errors soft down	errors soft up	Flux hard	errors hard downs	errors hard up	Flux all	errors all down	errors all up	Flux corr.	errors corr.
1	0.953	0.453	0.013	3.973	0.985	0.013	4.926	1.324	0.026	10.698	1.466
2	0.814	0.159	0.159	3.076	1.047	0.159	3.890	0.588	0.588	10.078	1.525
3	0.962	0.155	0.001	6.319	1.182	0.001	7.281	1.189	0.001	13.404	1.096
4	1.27	0.157	0.0005	7.10705	0.286	0.0005	8.380	0.375	0.032	15.837	0.384
5	1.819	0.144	0.013	8.500	0.286	0.013	10.319	0.369	0.054	21.165	0.433
6	1.260	0.1420	0.003	6.089	0.304	0.003	7.348	0.369	0.043	14.378	0.402

TABLE 3.5: Fluxes of HD168112 obtained with the 3T model. The units of fluxes and of their errors are $10^{-13} erg\ s^{-1} cm^{-2}$.

Obs.	Flux soft	errors soft down	errors soft up	Flux hard	errors hard downs	errors hard up	Flux all	errors all down	errors all up	Flux corrected	errors corrected
1	3.2895	0.6605	0.0375	13.232	0.95	0.95	16.521	1.200	1.200	31.544	2.2912
2	2.785	0.2668	0.2668	10.7185	0.5947	0.033	13.5035	0.449	0.449	28.641	0.9524
3	3.2068	0.0529	0.0189	12.3745	0.1305	0.0746	15.5815	0.1814	0.0626	30.198	0.2364
4	4.1341	0.298	0.0371	14.8395	0.4799	0.449	18.9735	0.9359	0.1213	37.866	1.0549
5	5.5351	0.53	0.0275	19.17	0.6152	0.2051	24.705	1.0642	0.1096	50.762	1.2059
6	4.2935	0.6085	0.6085	16.417	1.537	0.283	20.711	2.511	0.169	41.112	2.6599

TABLE 3.6: Fluxes of HD167971 obtained with the 3T model. The units of fluxes and o their errors are $10^{-13} erg\ s^{-1} cm^{-2}$ as well as their errors.

Now that we have the fluxes we can check if they follow as expected the 1/d relation for adiabatic wind interactions. We do this by means of a linear regression using the eq.3.1 with the corrected fluxes and accounting for their errors. The part $A \times \frac{a}{d}$ represents the emission of the wind-wind interaction and the parameter B the intrinsic emission. In this relation a is the semi-major axis of the orbit and d is the separation of the two stars at the specific orbital phase as given in the Table 2.6.

$$F_{corr} = A \times \frac{a}{d} + B \tag{3.1}$$

The linear regression was made with the polyfit function of the Python package numpy. We get for HD168112 the A parameter 3.768 ± 0.283, and for the B parameter 6.209 ± 0.803, both in the same units as the flux(i.e.$10^{-13} erg\ s^{-1} cm^{-2}$). The linear regression can be seen on the Fig.3.5.

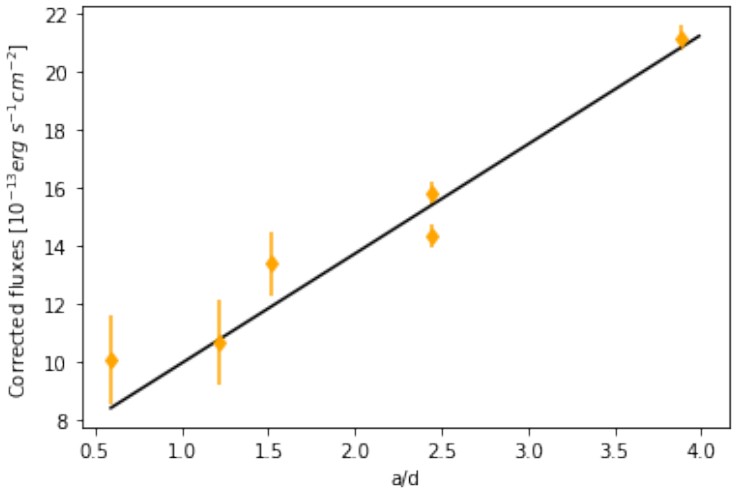

FIGURE 3.5: Linear regression assuming the corrected fluxes of HD168112 follow the relation 3.1. The relation was established using a/d rather than 1/d to have the same units for the coefficients A and B. The unit of fluxes are $erg\ s^{-1} cm^{-2}$

We clearly see the linear dependence expected. Using the relations described in Sect.2.2 between the phase and the true anomaly and thus the spatial distance between the stars, we plot the flux curve as a function of orbital phase (see Fig.3.6).

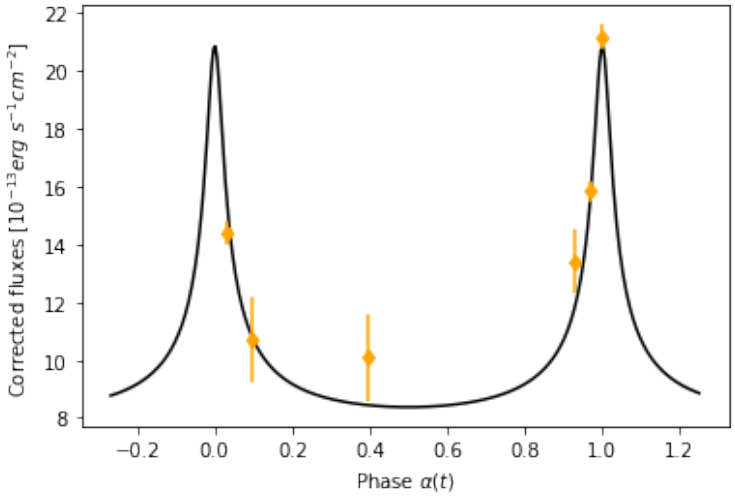

FIGURE 3.6: Modelling of flux as a function of the orbital phase of HD168112 with the observed corrected fluxes in orange dots.

Unfortunately, for HD167971, our data do not sample enough orbital phases of the outer orbit. Most of our observation fall near $\alpha = 0.7$. The single point near $\alpha = 0.3$ actually has the same a/d value as the group of points near $\alpha = 0.7$. Hence, we cannot test an a/d relation here. For the case of the inner binary, we only have data that cover half of the orbital phase values (α from $\sim$0.45 to $\sim$0.93). The Fig.3.7 represents the corrected fluxes observed as a function of the orbital phase.

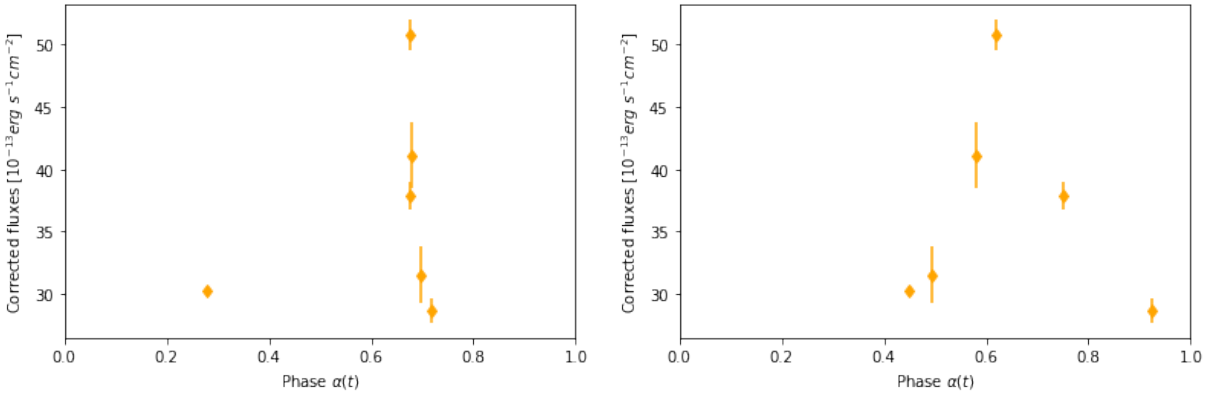

FIGURE 3.7: Corrected fluxes observed as a function of the outer orbital phase of HD167971 on the left, and of the inner orbital phase on the right.

However, what is interesting to observe, thanks to the last two figures, is that quite significant variations occur on a timescale consistent with the orbital period of the eclipsing binary rather than the long orbital cycle. In fact, the flux variation compared to the long cycle is too fast to be attributed to the interaction between the third component and the inner binary, as the distances between them don't change significantly (see Table 2.7). We will discuss more about the possible origins of this rapid variability in the Sect.4.

3.3 The cooling parameter

As explained in Sect.1.2, the cooling parameter will directly give an idea of which type of regime applies to the shock-heated plasma. Its expression is given by the eq.1.6. As previously, we will first develop the case of HD168112 and then move on to HD167971.

3.3.1 HD168112

To get the value of the cooling parameter χ several steps need to be done before. The first step is to obtain the spatial distance between each star and the shock zone. In order to get the distance, we easily solved the following system of equations (see Stevens et al. [1992]):

$$\eta = (\frac{\dot{M}_1 v_{\infty,1}}{\dot{M}_2 v_{\infty,2}})^{1/2} = \frac{d_1}{d_2} \tag{3.2}$$

$$d = d_1 + d_2 \tag{3.3}$$

When expressed in units 10^{12} cm, d_1 and d_2 provide respectively the parameter d_{12} of the eq.1.6 for the primary and the secondary star. The first equation implicitly assumes that the wind momentum equilibrium point and the shock are located at the same distance from the star. Thereafter, we consider d=a, where a is the semi-major axis of the orbit [Putkuri et al., 2023]. This work quotes the projected semi-major axis with i the inclination of the orbital plane with respect to our line of sight, asin(i) = 1004.7 $R_\odot$. Their orbital solution gives as well the mass of each star multiplied by $sin^3 i$, M$sin^3 i$ = 27.1±0.1 $M_\odot$ for the primary and M$sin^3 i$ = 24.6±0.3 $M_\odot$ for the secondary. Injecting in it the estimated masses for O4.5IV and for O5.5V stars given by Martins et al. [2005], permits to obtain an average inclination of 61.1°, and thus a semi-major axis equal to 1147 $R\odot$. The value used to calculate the χ and its result is given in Table 3.7. We note that we used the terminal velocity predicted by Muijres et al. [2012], as we assume the distance d_{12} to be large enough in the case of

HD168112 for the winds to reach their terminal velocities. Naturally, the value of χ changes according to the phase, this is why the χ at the periastron[1] is given as well, where the value of d and χ are at their lowest.

Parameters	Primary	Secondary
v_8	2.96	2.76
$\dot{M}_{-7}$	19.4	7.05
d_{12}	50.44	29.36
χ	199.61	241.69
$\chi_{periastron}$	51.34	62.17

TABLE 3.7: Where v_8 ,$\dot{M}_{-7}$, d_{12} are respectively the wind velocity in units of 1000 km s^{-1}, the mass-loss rate in units of 10^{-7} $M_\odot$ yr^{-1}, and the distance from the star to the contact discontinuity in units of 10^{12} cm. Mass loss rates and terminal velocities are taken from the work of Muijres et al. [2012].

From the above calculation, we see that the wind interaction zone of HD168112 is in the adiabatic regime and remains so all along the orbit.

3.3.2 HD167971

In the case of HD167971, the development follows the same reasoning as for HD168112 with the particularity that we have here a triple system. Which means that the cooling parameter will be calculated for the inner binary and then for the outer orbit. For the inner binary, the semi-major axis obtained by Ibanoglu et al. [2013] is 36.69± 0.20 $R_\odot$. For the external binary, the orbital solution parameters used are those calculated by Le Bouquin et al. [2017]. In the latter work, they give two ways to obtain the a parameter. We use here the approach based on Kepler's third law (eq.3.4).

[1] $\chi_{periastron} = \chi$(1-e)

Parameter	
i	35°
$K_1 + K_2$	28 kms^{-1}
P	674.438 10^6 s
e	0.443

TABLE 3.8: The orbital parameters of the outer orbit needed in order to compute the semi-major axis.

$$asini = \frac{(K_1+K_2)P\sqrt{1-e^2}}{2\pi} \quad (3.4)$$

Of course, the separation of the components of the binary is too short to expect the winds to reach their terminal velocity. In the interest of having a more realistic cooling parameter, the velocities were calculated following the eq.1.1 with the terminal velocities following the work of Howarth et al. [1997] and the stellar radius following the values of Muijres et al. [2012].The values used to compute χ and our results are given in Table 3.9.

Parameters	Primary A	Secondary B	AB	Third
v_8	2.377	2.594	2.486	2.921
$\dot{M}_{-7}$	2.477	1.419	3.896	3.258
d_{12}	1.425	1.127	235.932	235.932
χ	0.292	0.0440	2312.985	5271.8431

TABLE 3.9: Mass loss rates are taken from the work of Muijres et al. [2012].

From these calculations we find that the wind-wind collision in the inner binary is highly radiative, whereas the interaction between the wind of the binary and the third star is adiabatic.

3.4 Light curve

Light curves (LC) of each target have been extracted to check the variability on short time scales. The procedures to generate the LCs are similar to those in Sect.2.3 with the SAS program. The time bin taken was 500s with an energy range from 0.5 to 10.0 keV. LCs are

plots of the count rates against the time. We built an LC for each EPIC-instrument which means 16 LCs were extracted in total for each target. The variability test done consists firstly to compare each LC to a model assuming a constant count rate and computing the χ^2. Then we compared this last value to $\chi^2_{0.95}$ taken from a chi-squared distribution. That means if we have the case that $\chi^2 \geqslant \chi^2_{0.95}$, we have less than 5% probability that the signal is due to noise fluctuations about a constant count rate. The values computed are given in the Appendix in the Table 5.1 for HD168112, and in the Table 5.2 for HD 167971. Almost all values are below the threshold, which means that we cannot reject that the variability is due to noise. Only one value for each target stands out, both for the MOS 2 of the obs2. Nevertheless these values are not confirmed by the other instruments. Furthermore, for the case of HD167971, the EPIC-PN instrument shows an even lower probability while it receives more than twice the light recorded by the EPIC-MOS instruments.

3.5 X-ray luminosity

As the fluxes corrected for the ISM absorption were retrieved, the overall X-ray luminosity can be calculated using the eq.3.5. d is the distance between the Earth and the targets in cm. It equals approximately to 6.174×10^{21} cm ($\sim 2kpc$), following the Gaia parallax of HD168112, for both systems. We assume the same distance for HD167971 as we note that the ruwe[2] of the Gaia parallax of HD167971 is quite high indicating that this value is not reliable. We thus adopt the same distance as for HD168112 since both systems belong to the NGC6604 cluster. The bolometric luminosities used for HD 168112 are given by Putkuri et al. [2023]. They are about 1.679×10^{39} erg s^{-1} for the primary, and 1.303×10^{39} erg s^{-1} for the secondary. This provides a total bolometric luminosity of about 2.982×10^{39} erg s^{-1}. For HD167971, the bolometric luminosities used follow the work of Ibanoglu et al. [2013] for the primary and the secondary components, and the prediction of Martins et al. [2005] for the third star. In order, we have a value for the respective components equal to 0.929×10^{39} erg s^{-1},0.486×10^{39} erg s^{-1}, and 1.429×10^{39} erg s^{-1}, yielding a total bolometric luminosity of about 2.844×10^{39} erg s^{-1}.

$$L_X = 4\pi d^2 F_{corr} \tag{3.5}$$

[2]The ruwe (renomalized unit weight error) is a statistical number that gives an idea of the quality of an astrometric measurement.

Observation	L_X HD168112	L_X/L_{Bol} HD168112	L_X HD167971	L_X/L_{Bol} HD167971
1	5.124×10^{32}	1.718×10^{-7}	1.511×10^{33}	5.312×10^{-7}
2	4.827×10^{32}	1.619×10^{-7}	1.372×10^{33}	4.823×10^{-7}
3	6.420×10^{32}	2.153×10^{-7}	1.446×10^{33}	5.085×10^{-7}
4	7.586×10^{32}	2.544×10^{-7}	1.814×10^{33}	6.377×10^{-7}
5	1.0137×10^{32}	3.399×10^{-7}	2.431×10^{33}	8.548×10^{-7}
6	6.887×10^{32}	2.309×10^{-7}	1.969×10^{33}	6.923×10^{-7}

TABLE 3.10: The units of L_X are erg s^{-1}. L_X is evaluated over the 0.5-10 keV energy band.

Finally, the intrinsic X-ray luminosity of HD168112 can be evaluated from the B parameter found in Sect.3.2 which yields the intrinsic flux of HD168112. We obtain $L_{X,intrin} = 2.97 \times 10^{32}\,erg\,s^{-1}$ and $L_{X,intrin}/L_{bol} = 9.97 \times 10^{-8}$. This latter ratio is in perfect agreement with the canonical value near 10^{-7} obtained by Nazé [2009].

3.6 Colour Image

The name of this section is ambiguous because we will indeed construct a three-colours image but it will not represent the true colours of the systems. In fact, as is usually done when colour images are made from non-optical observations, we will match a colour to an energy range and merge it to obtain a 'true' colour image. Here we will create a "colour" image by combining observations from the EPIC instruments. The RGB processing method will be employed, whereby the colours red, green and blue will be associated with a range of energies/wavelengths. The colour red is associated with the 0.5 to 1 keV range, which represents the soft part of the spectrum. Green is used for the range from 1 to 2 keV, which represents the medium portion of the spectrum. The blue is associated with the hard part of the spectrum, spanning from 2 to 10 keV. The following section outlines the procedure for obtaining the final image.

1. Starting with the Obs 1, three images were generated for each EPIC instrument across the three aforementioned energy ranges. These images will be referred to as intermediate R, intermediate G, and intermediate B images. This step was completed

using the evselect command and the appropriate PI conditions. Additionally, an exposure map was generated for each image.

2. At this point, we have three images and three exposure maps per band. The first step in this process is to merge the exposure maps from the same band and normalise them. Subsequently, the intermediate R, G, and B images from the same band are merged and divided by the appropriate normalised exposure map. Now we have three images that can be associated with their colour. The resulting images will be designated as the R, G, and B images. Following these steps, a colour image can be produced for Obs 1 merging them together. It should be noted that these colour images will not be required for the final image.

3. Steps 1 and 2 are repeated for the other observations.

4. The final image is created by following a similar process to step 2. The R, G and B images of the different observation produced previously are combined in their band, then together and finally corrected with normalised exposure maps. These are derived from the combination of the previous exposure maps. The colour contrast of the final image can be adjusted by changing the weight given to the red, green or blue parts.

Although this is not our focus here in this work, we stress that Fig.3.8 reveals the existence of numerous secondary sources that are weaker than our targets. Many of them gather in the western part of the image, with some concentration of sources around HD167971. These sources most likely correspond to low-mass pre-main sequence stars belonging to the NGC 6604 cluster.

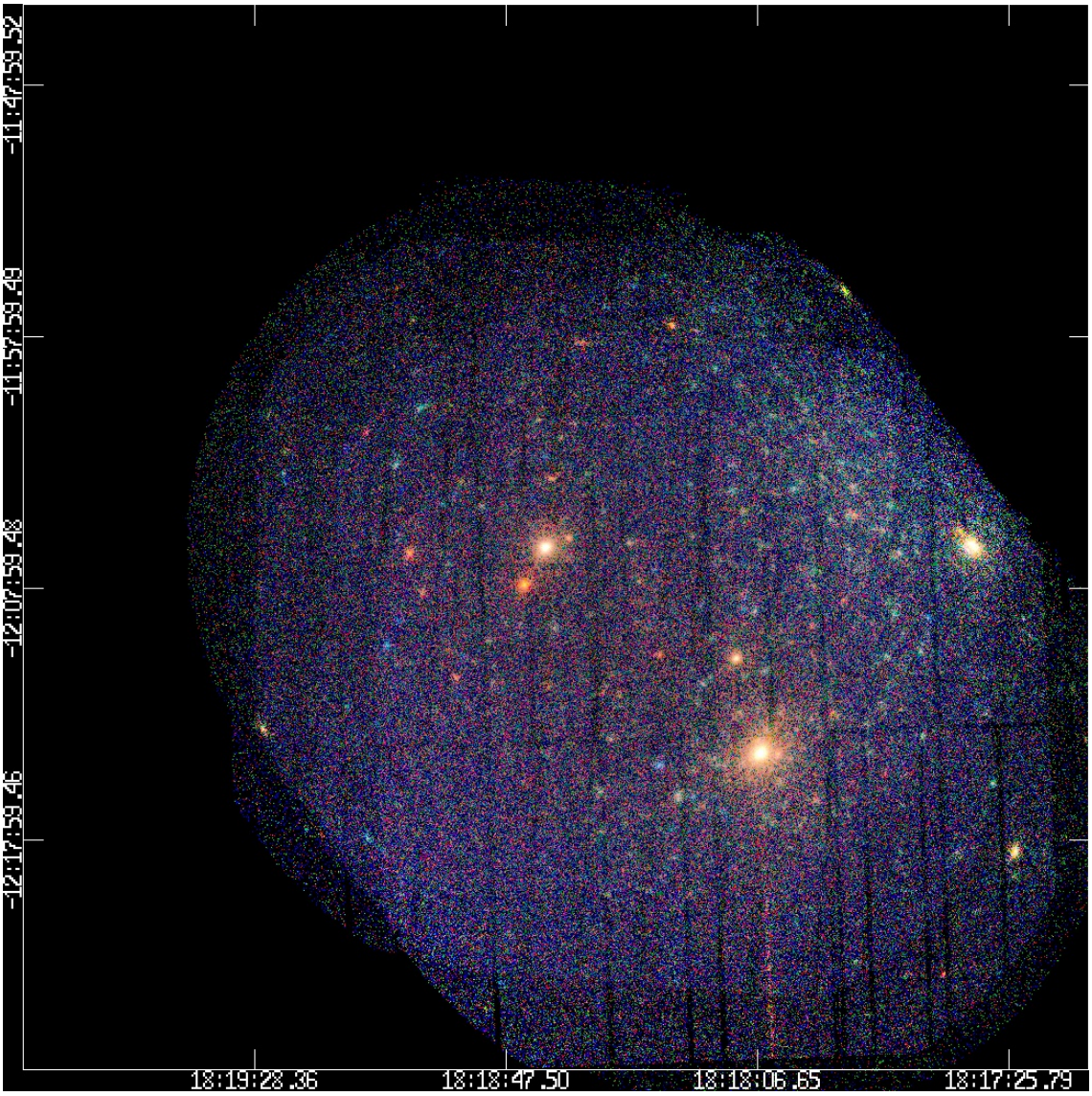

FIGURE 3.8: The final three colour image of HD168112, at the centre, and HD167971, in the lower right of the image. North is up and East is to the left.

Chapter 4

Discussion

4.1 Comparison with ROSAT observations

We compare our data set with two ROSAT observations. One of the ROSAT observations was taken using the Position Sensitive Proportional Counter (PSPC) instrument, and the other one using the High-Resolution Imager (HRI) instrument. The PSPC observations were collected between the 13th and 15th September 1993 (HD168112 phase ~ 0.0062, HD167971 outer orbit phase ~ 0.3). For the HRI, the observation was done in a fragmented way between the 12th Septempber 1995 and the 10th October 1995 (HD168112 phase ~ 0.45, HD167971 outer orbit phase ~ 0.39). After processing the PSPC data with xselect, we fitted our data with a model of one plasma temperature. We obtained the fit parameters and the flux (in the band 0.5-1keV) listed in the Table 4.1.

System	N_h^{circum}	kT_1 (keV)	N_1	Chi^2/dof	Flux
HD168112	1.25	0.24	4.74×10^{-2}	19.19/17	1.55×10^{-13}
HD167971	0.80	0.39	1.36×10^{-2}	15.62/17	3.78×10^{-13}

TABLE 4.1: Best-fit parameters for the spectra of HD168112 and HD167971 using the ROSAT PSPC observation.The units of fluxes are erg $s^{-1}cm^{-2}$.The absorption columns are given in $10^{22}cm^{-2}$. We recall the definition of N_1: the normalisation parameter which is given by $\frac{10^{-14}}{4\pi D_A^2}\int n_e n_H\, dV$ where D_A is the angular diameter distance to the source (cm), dV is the volume element (cm^3), and n_e and n_H are the electron and H densities (cm^{-3}).

For the HRI observation, we used the ROSAT HRI archive to get the count rate of the observation over the total band, then we obtained the fluxes using WebPIMMS, powered by

PIMMS v4.13a. This software allows converting the HRI count rate into a flux, provided that some model parameters are assumed for the spectrum. For the latter, we adopt the model parameters from the fits of the PSPC spectra. We can now plot the soft fluxes as a function of the phases including the ROSAT data (Table 4.1 for HD168112 and Table 4.2 for HD167971).

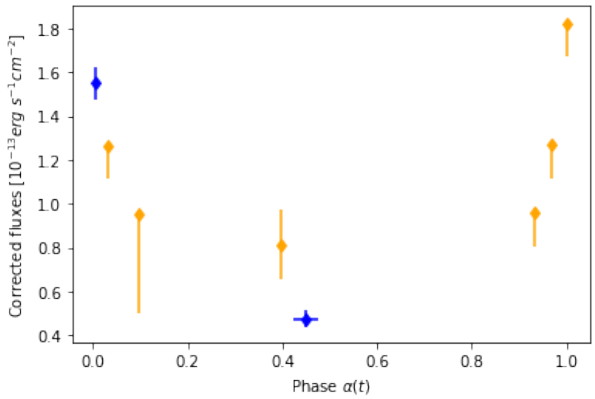

FIGURE 4.1: Soft fluxes observed for HD168112 as a function of the orbital phase. The blue dots represent the ROSAT data.

The observation of HD168112 with the PSPC corresponds perfectly to the model we found in Section3.2. The HRI data fall slightly below the level derived from the XMM data. This is very likely due to the method that we used to infer the flux of the HRI observation which is affected by huge uncertainties that are not well reflected by the formal error bar in Fig.4.1.

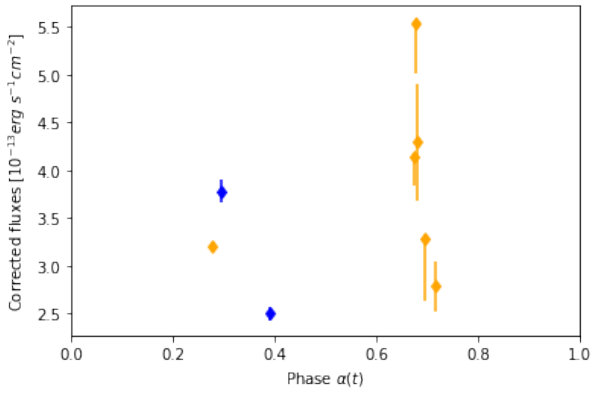

FIGURE 4.2: Soft fluxes observed for HD167971 as a function of the outer orbital phase. The blue dots represent the ROSAT data.

ROSAT data do not permit to get further information on HD167971.

4.2 Analysis of the fit parameter

One difficulty that affects our models is the degeneracy between the circumstellar absorption (N_H) and the plasma temperature (kT). This effect is most severe for the lowest temperature component. A model with a high N_H and a low plasma temperature and a other model with a lager kT but an absorption column smaller can both fit a same data set. This situation leads to the existence of local minima in the parameter space that result in nearly the same quality for the fit of the data. The solution that will emerge from the fitting routine is then mostly ruled by the specific realisation of the noise on the data.

One useful instrument for overcoming the limitations due to the degeneracy is the hardness ratio, which is the ratio between the flux of the hard band and those of the whole band. The Table 4.2 presents the values for the six observations of each system.

Obser.	HD168112	Phase	HD167971	Phase int.	Phase ext.
Obs 1	0.81	0.096	0.80	0.493	0.697
Obs 2	0.79	0.396	0.79	0.925	0.717
Obs 3	0.87	0.931	0.79	0.448	0.278
Obs 4	0.85	0.968	0.78	0.751	0.675
Obs 5	0.82	0.999	0.78	0.620	0.678
Obs 6	0.83	0.032	0.79	0.580	0.680

TABLE 4.2: The hardness ratios of all observations were calculated using the fluxes provided in Tables 3.5 & 3.6. The phases are additionally indicated for the purpose of relating the ratio to the target configurations.

Regarding the analysis of the fit parameters listed for HD167971 in the Table 3.4. Upon initial examination, it can be observed that the maximum plasma temperature remains relatively consistent for the majority of observations, taking into account the associated errors. It is noteworthy that Obs 1 exhibits a distinctive value in comparison to the others. However, the kT_3 parameter of this observation exhibits large uncertainty. The hardness ratio for the Obs 1 demonstrates minimal variation in comparison to the others, despite an expected increase in line with a higher plasma temperature. This provides insufficient

justification for focusing on this value.

With regard to the circumstellar absorption parameter, it can be observed that all the observations exhibit values that are relatively similar, taking into account the associated errors. The observation that is slightly divergent from the others is the fifth. This reduction should result in a decrease in the hardness ratio, given that fewer soft rays are absorbed, thereby increasing the flux in the soft energy band. The consistency of the hardness ratio with the others may indicate that the NH value is attributable to a local minimum.

The final point to be addressed with regard to the fitting of HD167971 is the data from the emitter plasma for the lowest temperature. It is notable that the kT_1 of Obs 2 is the lowest, being almost twice that of the other observations. However, the most significant finding is the amount of matter expressed via the emission measure parameter N_1. The model provides an N_1 value of approximately eight times greater than the other values. Even when the low errors are taken into consideration, an emitting quantity almost four times greater remains. It is important to recall that the second observation is the one where the flux of HD 167971 is the lowest and corresponds to an eclipse of the inner binary system. As a result, this value may potentially be due to the geometry of the system, where part of the warmer regions may be masked and reveal more extended colder regions.

Let us now proceed to an analysis of the HD168112 fit parameters, listed in the Table 3.2. A preliminary examination of the model's temperatures reveals an unexpected outcome: the highest value is not observed at periastron (Obs 5), contrary to expectations. Actually, it is the lowest value observed. Indeed, the third observation exhibits the maximum temperature, with a kT3 that is almost 2.5 times higher than that observed at the periastron. The highest hardness ratio observed, from the Obs 3, confirms this increase. Nevertheless, the temperature in question is subject to very large uncertainties and the error command yields meaningless error estimates. This situation indicates that the higher plasma temperature of the model is not constrained by the data for this observation. Furthermore, a comparison of the 2T model parameters for Obs 3 reveals that the model has converged to a considerably lower temperature. Those results indicate that the parameter space for HD168112 is highly complex, and that some of the model parameters are not well constrained by the fits of the data. This phenomenon can be attributed to a number of factors, including the presence of a highly degenerate parameter space or an insufficient quality of data. Additionally,

the second observation exhibits a higher temperature in comparison to Obs 1, 4, 5, and 6. However, given the hardness ratio and the fact that we have outlier errors there too, the Nh/kT degeneracy appears to be the most plausible explanation.

We will now turn our attention to on the final three observations. It would be prudent to exercise greater caution than was previously the case in analysing the data for kT_3. The value provided by the 3T model is, indeed, slightly lower for the observation 5. However, when the errors are taken into account, all three observations are found to be similar. Furthermore, additional arguments allow the possibility of a decline in temperature at periastron. Firstly, a comparison with the 2T model demonstrates that the fifth observation continues to exhibit the lowest temperature, and the error margins are even less pronounced. Secondly, an examination of the hardness ratios reveals that the lowest value is observed at the periastron. Thirdly, as stated in the Sect.3.1.1, the spectral fit of Obs 5 does not exhibit the anticipated Fe XXV line, in contrast to Obs 4. This suggests that Obs 4 may be associated with a hotter plasma than Obs 5. While these arguments should be considered carefully, they suggest that the observed low value of kT_3 at the periastron is not an artefact of the model. One potential explanation to this issue may lie in the phenomenon of radiative braking. It is conceivable that this effect, which is most pronounced when the stars are in closest proximity, could be a contributing factor. Moreover, even if the system remains in an adiabatic state at periastron (see Sect.1.6), as the interaction zone contracts, recombinations may become more effective, leading to a reduction in plasma temperature.

Let us now turn our attention to the normalisation parameter N_1 which represents the quantity of matter emitting X-rays at the corresponding plasma temperature. For both systems, it can be discerned that N_1 is considerably larger than N_2 and N_3, and that N_2 and N_3 are relatively similar. Therefore, only a minor proportion of the plasma is heated to an exceedingly high temperature. This is consistent with the explanation provided in the introduction regarding the disparate temperatures observed in the wind interaction zone. In fact, the maximum temperature is observed in the zone corresponding to a head-on collision of the winds at the centre of the two shocks.

4.3 Part of the answer for non-overluminous CWBs

An important open question related to the CWB phenomenon is the lack of a clear X-ray overluminosity for a majority of the massive binaries. On closer inspection of the data presented, it becomes evident that a potential solution can be identified for wide binaries similar to HD168112. Upon further examination of the Fig.3.6, we can see that the X-ray flux from the wind interaction dominates the lightcurve and thus the observed luminosity over only a small part of the orbit. To be more specific, let's consider that a system is overluminous when its X-ray luminosity is twice the intrinsic value L_X/L_{Bol}. Using the value calculated in the Sect.3.5, we can establish that the system is qualified as overluminous when the corrected fluxes are higher than 12.42 $\times 10^{-13} erg\ s^{-1} cm^{-2}$. This is equivalent to a system configuration in which the phase is ± 0.06 with respect to the periastron. The Fig.4.3 shows the flux graph as a function of phase, highlighting the areas considered to be overluminious.

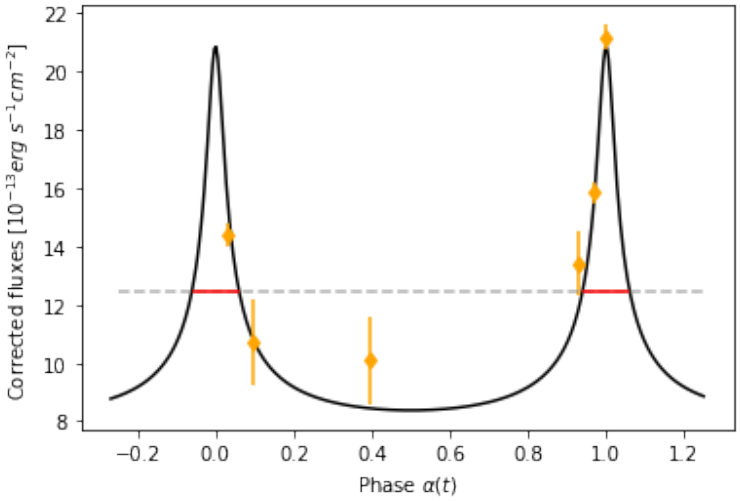

FIGURE 4.3: Modelling of flux as a function of the orbital phase of HD168112. The orange dots correspond to the observed corrected fluxes. The dashed line represents the limit we consider over which the X-ray emission of the system is overluminous. The red part highlights the moment when the system's observations will reveal the phenomenon.

It can therefore be surmised that the system is considered to be overrluminous only over 12% of its orbit. Consequently, it can be posited that the probability of randomly observing CWBs with excess luminosity, as observed in the surveys, is exceedingly low for similar binary systems.

4.4 Perspective

The results and the discussion of this work have left some prospects open for the study of these two systems. For HD168112, as explained in the analysis of the fitting parameter, the model does not constrain the data very well. This is not a problem for our study because we are concentrating on fluxes analysis. However, further work on the fit could be carried out to obtain more stringent constraints on the temperature stratification of the wind interaction zone. Such constraints might be within reach of future observatories such as Athena that will offer the possibility to collect high-resolution spectroscopy including at photon energies above 6 keV where the colliding wind emission dominates. This will provide more accurate constraints on the temperature variations as a function of orbital phase.

For the inner orbit of HD167971, in order to obtain a complete X-ray light curve, it is necessary to get observation in the first half of its orbital cycle. This will permit a comprehensive investigation into the origin of the observed variation. As outlined in Sect.1.2, the variation in X-ray fluxes observed in CWBs in the case of eclipsing binaries can be attributed to changes in optical depth along the line of sight. It results of the stars orbital motion. Furthermore, as the wind interaction zone of the inner binary of HD167971 is in the radiative regime, the system is more sensitive to the various instabilities outlined in Sect.1.2. Moreover, studying this system will enable us to gain insights into the influence of gravity and orbital motion, and consequently of Coriolis deflection, on the flux emitted. This last phenomenon results in deflection of the stellar winds and modification of the shape and structure of the collision region. The collisions between the stellar winds are no longer symmetrical. The influence of this phenomenon may be discerned within our data set. A comparison of our fluxes with the optical light curve obtained by reference Mayer et al. [2010] reveals a phase shift between the two (see the Fig.4.4).

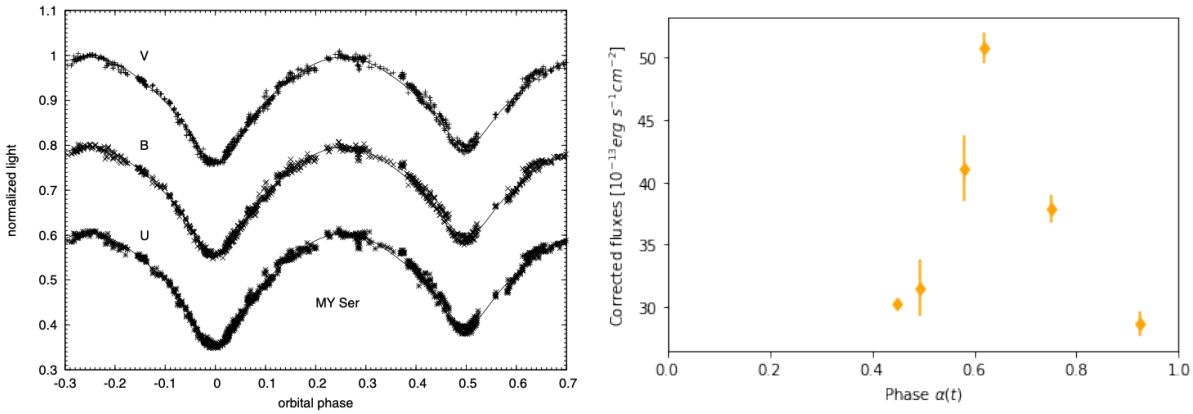

FIGURE 4.4: UBV observations with theoretical curves taken from Mayer et al. [2010] on the left. Our corrected fluxes observed on the right.

Chapter 5

Conclusion

This master thesis studied the study of the colliding wind binaries focusing on two O-type systems: HD168112 and HD167971. The main goal was to describe their X-ray behaviour with a set of six XMM-Newton's observations over a period of two decades. After processing our data set, we attempt to fit the spectra with models using absorption components related to the interstellar medium and the winds, combined with optically thin thermal plasma models. The model TBabs*phabs*(apec+apec+apec) has been selected for our result. We assumed three temperatures of the emitting plasma, and found that this model usually does a better job than a model assuming two plasma temperatures. Using the 3T model for each system, we obtained a set of fit parameters for each observation hence of their spectra in which some emission lines have been identified. From this model we retrieved the fluxes which permit us to achieve our goal. These fluxes have been calculated in three different energy ranges: one in the soft part of the spectrum (from 0.5 to 1 keV), then in the harder part (from 1 to 10 keV), and finally taking into account the full energy range (from 0.5 to 10 keV). Then, we obtain the fluxes corrected from the ISM absorption from 0.5 to 10 keV. Here are the main result for HD18112:

- The well-distributed observations along its orbital cycle permitted us to perform a linear regression on the corrected fluxes F_{corr}. We assumed that $F_{corr} = A \times \frac{a}{d} + B$. This finding aligned perfectly with our data, confirming that X-ray emission follows the 1/d relationship for wide binaries, as previously hypothesised. The A parameter we get equals to 3.768 ± 0.283, and for the B parameter to 6.209 ± 0.803, both in the same units as the flux(i.e.$10^{-13} erg\ s^{-1} cm^{-2}$). Two ROSAT observations confirmed this result.

- The calculations of the cooling parameters permitted to determine that HD168112 is in an adiabatic regime all along its orbit.

- Using the corrected fluxes we obtain the X-ray luminosity. With the parameter B calculated above, we get the intrinsic X-ray luminosity. We obtained $L_{X,intrin} = 2.97 \times 10^{32}\,erg\,s^{-1}$ and $L_{X,intrin}/L_{bol} = 9.97 \times 10^{-8}$. This finding is in perfect agreement with the canonical value near 10^{-7} obtained by many previous studies, such as Nazé [2009].

- Assuming that the system was over-luminous when we had twice the $L_{X,intrin}/L_{bol}$, we can posit a partial answer to the question of the lack of over-luminosity of certain CWBs. In fact, HD168112 is only over-luminous for 12% of its orbital phase. If we consider that the wide orbits resemble this system, the probability of observing an over-luminous system at random is rather low.

- Analysis of its fit parameters highlights how highly complex is the parameter space for HD168112. In addition, a number of arguments have demonstrated that a slight reduction in the temperature of the emitting plasma at the periastron may occur, contrary to expectations. We attributed it to the phenomenon of radiative braking and to an enhancement of the recombination as the interaction zone contracts.

Here are the main result for HD167971:

- The calculations of the cooling parameters permitted to determine that the wind interaction zone of the inner binary is in a radiative regime all along its orbit. For the outer binary, we have determined that the adiabatic case also applies throughout its orbit.

- In opposition of HD168112, the observations are not well distributed along the orbital phases. This does not allow us to run a linear regression on the fluxes. Nevertheless, the plots of the flux as a function of the long and short period shows that the variation is rather shaped by the eclipsing binary than by the long orbital cycle. In fact, the flux variation rate compared to the long cycle is too fast to be attributed to the interaction between the third component and the inner binary.

- The space parameter seems to be simpler than the one of HD168112. Which implies that the model parameters are well constrained by the fits of the data.

It becomes evident that the number of results returned for HD168112 is considerably higher than that for HD167971. This is due to the lack of observations along both the long and short periods. It is therefore imperative that new observations be made in order to undertake a more thorough study of HD167971, especially for the eclipsing binary. An investigation

of the inner binary will facilitate the acquisition of insights into the impact of gravity and orbital motion, and thereby of Coriolis deflection, on the observable flux.

Appendix

This appendix provides the comparative table used for the variability test made on the light curves. We compared our χ^2 to $\chi^2_{0.95}$ taken from a chi-squared distribution Thompson [1941]. Subsequently, spectra of the T2 model of HD 168112 and HD167971 are presented.

Obs 1	χ^2_{red}	DOF	χ^2		$\chi^2_{0.95}$
MOS1	1.58	17	26.865	$<$	27.6
MOS1	0.74	17	12.660	$<$	27.6
Obs 2	χ^2_{red}	DOF	χ^2		$\chi^2_{0.95}$
MOS1	0.78	25	19.5	$<$	37.7
MOS2	1.51	25	37.699	$\approx$	37.7
Obs 3	χ^2_{red}	DOF	χ^2		$\chi^2_{0.95}$
MOS1	1.11	47	52.252	$<$	63.99
MOS2	0.67	45	30.15	$<$	61.65
PN	0.63	46	28.98	$<$	62.82
Obs 4	χ^2_{red}	DOF	χ^2		$\chi^2_{0.95}$
MOS1	0.81	23	52.252	$<$	35.2
MOS2	0.67	23	30.150	$<$	35.2
PN	1.34	23	28.980	$<$	30.1
Obs 5	χ^2_{red}	DOF	χ^2		$\chi^2_{0.95}$
MOS1	1.03	21	21.63	$<$	32.7
MOS2	1.06	21	22.26	$<$	32.7
PN	0.71	17	12.07	$<$	27.6
Obs 6	χ^2_{red}	DOF	χ^2		$\chi^2_{0.95}$
MOS1	0.89	21	18.69	$<$	32.7
MOS2	0.97	21	20.37	$<$	32.7
PN	0.97	17	16.49	$<$	27.6

TABLE 5.1: Values used for the variability test of the Sect.3.4 of HD168112. DOF is the degree of freedom.

Obs 1	χ^2_{red}	DOF	χ^2		$\chi^2_{0.95}$
MOS1	1.01	17	17.17	$<$	27.6
MOS2	1.25	17	21.196	$<$	27.6
Obs 2	χ^2_{red}	DOF	χ^2		$\chi^2_{0.95}$
MOS1	1.29	25	32.170	$<$	37.7
MOS2	1.46	25	36.620	$\sim$	37.7
PN	0.65	22	14.3	$<$	33.9
Obs 3	χ^2_{red}	DOF	χ^2		$\chi^2_{0.95}$
MOS1	0.86	47	40.42	$<$	63.99
MOS2	1.04	45	46.8	$<$	61.65
PN	1.09	46	50.14	$<$	62.82
Obs 4	χ^2_{red}	DOF	χ^2		$\chi^2_{0.95}$
MOS1	1.27	23	29.176	$<$	35.2
MOS2	0.96	23	22.08	$<$	35.2
PN	1.04	19	19.76	$<$	30.1
Obs 5	χ^2_{red}	DOF	χ^2		$\chi^2_{0.95}$
MOS1	1.42	21	29.800	$<$	32.7
MOS2	0.92	21	19.320	$<$	32.7
PN	0.96	17	16.320	$<$	27.6
Obs 6	χ^2_{red}	DOF	χ^2		$\chi^2_{0.95}$
MOS1	0.89	21	18.27	$<$	32.7
MOS2	0.68	21	14.28	$<$	32.7

TABLE 5.2: Values used for the variability test of the Sect.3.4 of HD167971. DOF is the degree of freedom.

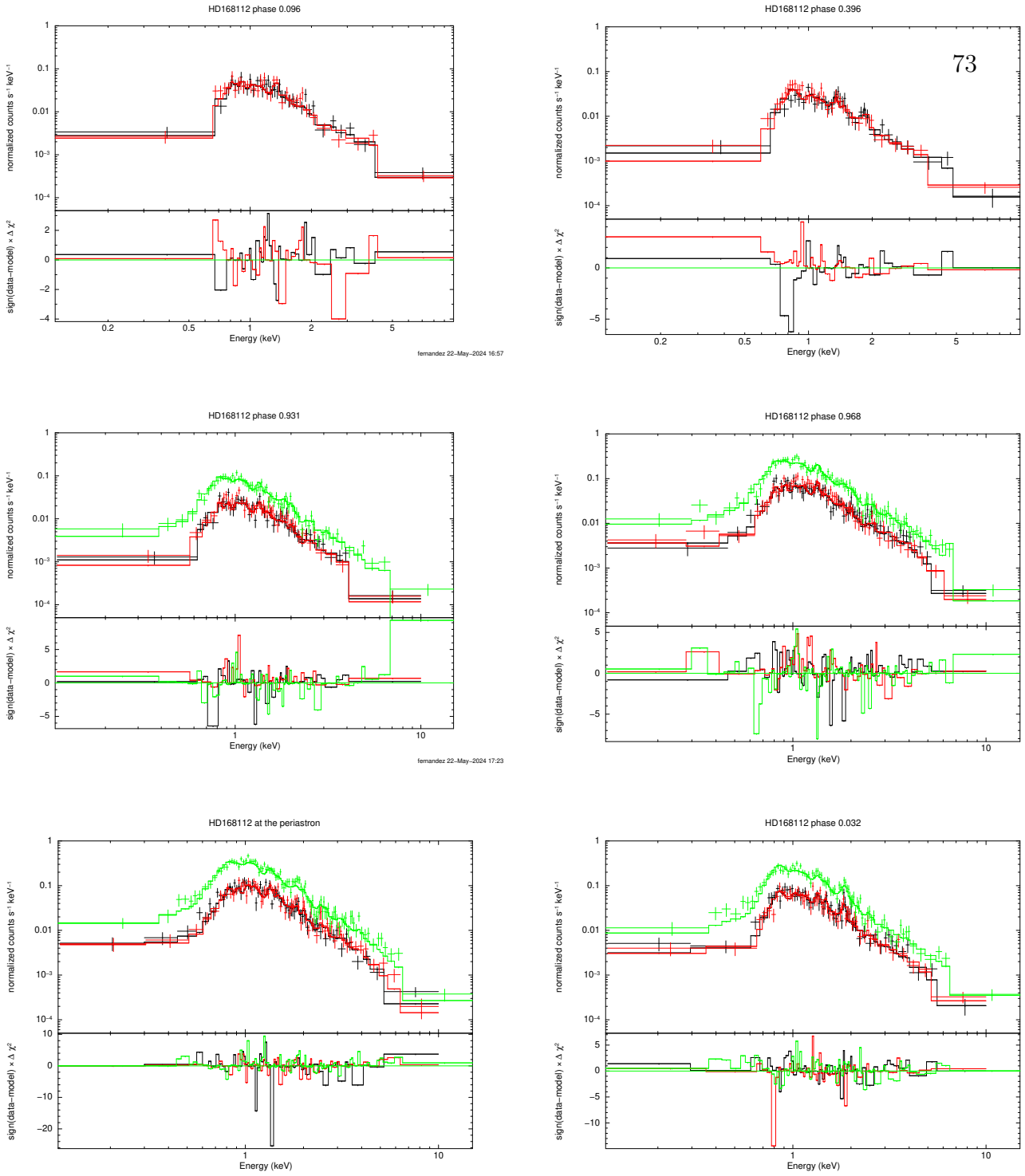

FIGURE 5.1: EPIC-MOS1 (in black), EPIC-MOS2 (in red) and EPIC-PN (in green) spectra of HD168112 in the case of the 2T model for the 6 observations. In the lower part of each graph, the deviation of the data set in comparison to the model is shown. From top left to bottom right, the different panels correspond to observations 1, 2, 3, 4, 5 and 6.

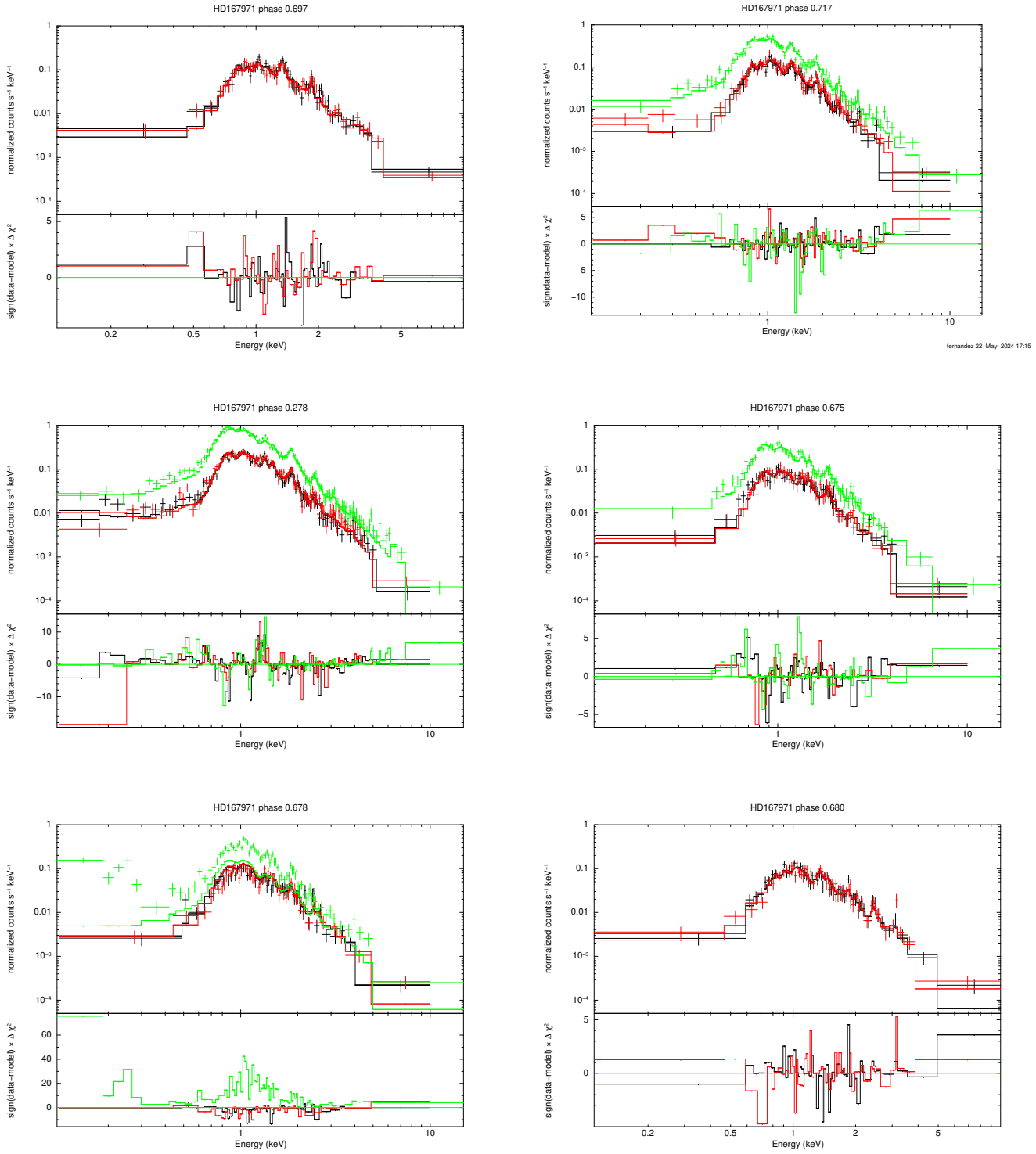

FIGURE 5.2: Same as Fig.5.1, but for the 2T models fitted to the spectra of HD167971.

Bibliography

M. Asplund, N. Grevesse, A. J. Sauval, and P. Scott. The Chemical Composition of the Sun. , 47(1):481–522, Sept. 2009. doi: 10.1146/annurev.astro.46.060407.145222.

R. Blomme, S. Van Loo, M. De Becker, G. Rauw, M. Runacres, D. S. Gunawan, and J. Chapman. Non-thermal radio emission from o-type stars-i. hd 168112. *Astronomy & Astrophysics*, 436(3):1033–1040, 2005.

R. Blomme, M. De Becker, M. Runacres, S. Van Loo, and D. S. Gunawan. Non-thermal radio emission from o-type stars-ii. hd 167971. *Astronomy & Astrophysics*, 464(2):701–708, 2007.

R. Blomme, G. Rauw, D. Volpi, Y. Nazé, and M. Abdul-Masih. The colliding-wind binary hd 168112. *arXiv preprint arXiv:2405.03247*, 2024.

R. C. Bohlin, B. D. Savage, and J. Drake. A survey of interstellar hi from l-alpha absorption measurements. ii. *Astrophysical Journal, Part 1, vol. 224, Aug. 15, 1978, p. 132-142. Research supported by the Lockheed Independent Research Program;*, 224:132–142, 1978.

M. De Becker and V. Van Grootel. Interstellar medium course, 2023.

M. De Becker, H. Sana, O. Absil, J.-B. Le Bouquin, and R. Blomme. The long-period eccentric orbit of the particle accelerator HD 167971 revealed by long baseline interferometry *. *Monthly Notices of the Royal Astronomical Society*, 423(3):2711–2717, 06 2012. ISSN 0035-8711. doi: 10.1111/j.1365-2966.2012.21081.x. URL https://doi.org/10.1111/j.1365-2966.2012.21081.x.

J. R. Ducati. VizieR Online Data Catalog: Catalogue of Stellar Photometry in Johnson's 11-color system. CDS/ADC Collection of Electronic Catalogues, 2237, 0 (2002), Jan. 2002.

European Space Agency. Xmm-newton science operations centre, 2024. URL https://www.cosmos.esa.int/web/xmm-newton. Accessed: 01-August-2024.

S. Gudennavar, S. Bubbly, K. Preethi, and J. Murthy. A compilation of interstellar column densities. *The Astrophysical Journal Supplement Series*, 199(1):8, 2012.

I. D. Howarth, K. W. Siebert, G. A. J. Hussain, and R. K. Prinja. Cross-correlation characteristics of OB stars from IUE spectroscopy. *Monthly Notices of the Royal Astronomical Society*, 284(2):265–285, 01 1997. ISSN 0035-8711. doi: 10.1093/mnras/284.2.265. URL https://doi.org/10.1093/mnras/284.2.265.

C. Ibanoglu, Çakırlı, and E. Sipahi. MY Serpentis: a high-mass triple system in the Ser OB2 association. *Monthly Notices of the Royal Astronomical Society*, 436(1):750–758, 09 2013. ISSN 0035-8711. doi: 10.1093/mnras/stt1616. URL https://doi.org/10.1093/mnras/stt1616.

Jansen, F., Lumb, D., Altieri, B., Clavel, J., Ehle, M., Erd, C., Gabriel, C., Guainazzi, M., Gondoin, P., Much, R., Munoz, R., Santos, M., Schartel, N., Texier, D., and Vacanti, G. Xmm-newton observatory* - i. the spacecraft and operations. *AA*, 365(1):L1–L6, 2001. doi: 10.1051/0004-6361:20000036. URL https://doi.org/10.1051/0004-6361:20000036.

J.-B. Le Bouquin, H. Sana, E. Gosset, M. De Becker, G. Duvert, O. Absil, F. Anthonioz, J.-P. Berger, S. Ertel, R. Grellmann, et al. Resolved astrometric orbits of ten o-type binaries. *Astronomy & Astrophysics*, 601:A34, 2017.

C. Leitherer, D. Forbes, A. Gilmore, J. Hearnshaw, G. Klare, J. Krautter, H. Mandel, O. Stahl, W. Strupat, B. Wolf, et al. Photometry and spectroscopy of the o-type variable hd 167971. *Astronomy and Astrophysics (ISSN 0004-6361), vol. 185, no. 1-2, Oct. 1987, p. 121-130.*, 185:121–130, 1987.

F. Martins, D. Schaerer, and D. J. Hillier. A new calibration of stellar parameters of galactic o stars. *Astronomy & Astrophysics*, 436(3):1049–1065, 2005.

P. Mayer, H. Božić, R. Lorenz, and H. Drechsel. Sixty four nights of ubv photometry of early-type stars at la sila. *Astronomische Nachrichten*, 331(3):274–281, 2010. doi: https://doi.org/10.1002/asna.200911303. URL https://onlinelibrary.wiley.com/doi/abs/10.1002/asna.200911303.

L. Muijres, J. S. Vink, A. de Koter, P. Müller, and N. Langer. Predictions for mass-loss rates and terminal wind velocities of massive o-type stars. *Astronomy & Astrophysics*, 537:A37, 2012.

Y. Nazé. Hot stars observed by xmm-newton-i. the catalog and the properties of ob stars. *Astronomy & Astrophysics*, 506(2):1055–1064, 2009.

J. M. Pittard and B. Dawson. Colliding stellar winds structure and X-ray emission. , 477 (4):5640–5645, July 2018. doi: 10.1093/mnras/sty1025.

C. Putkuri, R. Gamen, N. I. Morrell, J. Maíz Apellániz, J. I. Arias, S. Simón-Díaz, G. A. Ferrero, C. N. Rodríguez, A. Sota, O. G. Benvenuto, and R. H. Barbá. The spectroscopic orbit of HD 168112 A,B in NGC 6604: another massive binary target for interferometry. *Monthly Notices of the Royal Astronomical Society*, 525(4):6084–6096, 09 2023. ISSN 0035-8711. doi: 10.1093/mnras/stad2657. URL https://doi.org/10.1093/mnras/stad2657.

G. Rauw. High energy course, 2022.

G. Rauw. Celestial mechanics, 2023.

G. Rauw. X-ray emission of massive stars and their winds. In *Handbook of X-ray and Gamma-ray Astrophysics*, pages 3185–3215. Springer, 2024.

G. Rauw and Y. Nazé. X-ray emission from interacting wind massive binaries: A review of 15 years of progress. *Advances in Space Research*, 58:761–781, 2015. URL https://api.semanticscholar.org/CorpusID:53455160.

H. Sana, S. E. de Mink, A. de Koter, N. Langer, C. J. Evans, M. Gieles, E. Gosset, R. G. Izzard, J. B. Le Bouquin, and F. R. N. Schneider. Binary Interaction Dominates the Evolution of Massive Stars. *Science*, 337(6093):444, July 2012. doi: 10.1126/science.1223344.

I. R. Stevens, J. M. Blondin, and A. Pollock. Colliding winds from early-type stars in binary systems. *Astrophysical Journal, Part 1 (ISSN 0004-637X), vol. 386, Feb. 10, 1992, p. 265-287.*, 386:265–287, 1992.

C. M. Thompson. Table of percentage points of the χ 2 distribution. *Biometrika*, 32(2): 187–191, 1941.